

# **Sympathetic nerve–fibroblast crosstalk drives nerve injury, fibroblast activation, and matrix remodeling in pancreatic cancer**

**Authors:** Ariana L. Sattler <sup>1,2</sup>, Parham Diba <sup>3</sup>, Kevin Hawthorne <sup>4</sup>, Carl Pelz <sup>4,5</sup>, Joe Grieco <sup>1</sup>, Tetiana Korzun <sup>3,6</sup>, Bryan Chong <sup>1</sup>, M.J. Kuykendall <sup>1</sup>, Rosalie C. Sears <sup>4,5</sup>, Daniel L. Marks <sup>7</sup>, Mara H. Sherman <sup>8</sup>, Teresa A. Zimmers <sup>2,5</sup>, S. Ece Eksi <sup>1,2,3,9</sup>

## **Affiliations:**

1. Cancer Early Detection Advanced Research Center (CEDAR), Knight Cancer Institute, Oregon Health and Science University, Portland, OR, USA
2. Department of Cell, Developmental, and Cancer Biology, Knight Cancer Institute, Oregon Health & Science University, 2720 S Moody Avenue, Portland, OR, 97201, USA
3. Department of Biomedical Engineering, Oregon Health & Science University, 3303 SW Bond Avenue, Portland, OR, 97239, USA
4. Department of Molecular and Medical Genetics, Oregon Health & Science University, Portland, Oregon
5. Brenden-Colson Center for Pancreatic Care, Oregon Health & Science University, Portland, OR, USA
6. Department of Pharmaceutical Sciences, College of Pharmacy, Oregon State University, 2730 S Moody Avenue, Portland, OR, 97201, USA
7. Endevisa Bio, Northbrook, Illinois, USA
8. Cancer Biology & Genetics Program, Memorial Sloan Kettering Cancer Center, New York, NY, USA.
9. Division of Oncological Sciences, Knight Cancer Institute, Oregon Health & Science University, Portland, OR, USA

**Keywords:** Cancer Neuroscience, Pancreatic Cancer, Cancer-Associated Fibroblasts, Sympathetic Nerves, Tumor Microenvironment

## **Abstract:**

Pancreatic cancer is a highly innervated gastrointestinal disease in which sympathetic nerves play a critical role in modulating tumor growth and the tumor microenvironment (TME). While recent studies suggest that sympathetic nerves influence various TME components, including lymphoid and myeloid immune cells, their interactions with cancer-associated fibroblasts (CAFs) remain poorly understood. CAFs are a hallmark of pancreatic tumors and are known to upregulate axon guidance and neuroactive cues, suggesting a potential feedback loop with tumor-innervating nerves. Here, we investigated the bidirectional crosstalk between sympathetic nerves and CAFs in human and mouse pancreatic tumors. Using a chemo-genetic ablation model, we selectively eliminated pancreatic sympathetic nerves and found that denervation significantly reduced tumor size in female mice. To further dissect this interaction, we established co-culture systems with immortalized pancreatic fibroblasts and primary sympathetic neuron explants, identifying key transcriptional changes driven by CAF-sympathetic nerve signaling. Our findings demonstrated that sympathetic signaling enhanced CAF activation and extracellular matrix remodeling, while activated CAFs, in turn, induced transcriptional programs in sympathetic neurons associated with nerve injury response. These results establish CAFs as central mediators of the tumor-supportive role of sympathetic nerves, offering further insights into the neural regulation of pancreatic cancer progression.

## **Introduction:**

Pancreatic ductal adenocarcinoma (PDAC) is an aggressive malignancy with a dismal prognosis, sustained by a dynamic and heterogeneous tumor microenvironment (TME) that promotes tumor progression (1). PDAC is a neurotrophic cancer characterized by extensive tumor innervation (2), including sensory (3), parasympathetic (4), and sympathetic (5) nerves, which collectively contribute to disease initiation, progression, and metastasis. Growing evidence links tumor-innervating nerves to adverse clinical outcomes in PDAC (6–8). Sympathetic nerves, which regulate the “fight-or-flight” response, can react rapidly to acute physiological stressors and adapt to chronic conditions such as cancer (9). Current evidence suggests that sympathetic signaling and associated adrenergic receptors contribute to PDAC initiation and progression (5, 10). Sympathetic nerves begin accumulating in the early stages of pancreatic cancer, known as pancreatic intraepithelial neoplasia (PanIN), and increase in density in higher-grade tumors (5). Norepinephrine (NE), the predominant sympathetic neurotransmitter, along with other sympathetic-associated signaling, can directly induce several tumor-promoting phenotypes, including cellular metabolic reprogramming (11), proliferation (12), and invasion (7, 12). Furthermore, adrenergic signaling from sympathetic nerves directly promotes CD8+ T cell exhaustion and immune suppression in PDAC (13). However, the specific influences of sympathetic nerves on other components of the TME, including the extracellular matrix (ECM), endothelial cells, immune

cells, and cancer-associated fibroblasts (CAFs), require further investigation. Importantly, a recent study implicates CAFs as a significant cellular partner in crosstalk with PDAC-innervating nerves (14), but the specific nature and consequences of these interactions remain unclear.

Originating from tissue-resident fibroblasts, tumor-infiltrating mesenchymal stem cells, and pancreatic stellate cells (PSCs) (15), CAFs become activated in the context of cancer and compose up to 80% of a PDAC tumor (16). Their diverse origins, as well as intratumor signaling gradients, contribute to their heterogeneity (17) and the acquisition of CAF phenotypes, including inflammatory (iCAF), myofibroblast (myCAF) (18), and antigen-presenting (apCAF) (19). Although their functions may vary with cancer stage and phenotype, CAFs directly support tumor cell growth and metabolism (20, 21), epithelial-to-mesenchymal transition (EMT) (22), and treatment responses by secreting tumor growth factors, chemokines, and cytokines (17). Furthermore, CAFs promote angiogenesis (23) and ECM deposition and remodeling (24), thereby contributing to PDAC progression. CAFs play a critical role in managing multiple aspects of the TME, and their role in facilitating sympathetic innervation remains under investigation. Recent work in colorectal cancer supports the significance of crosstalk between sympathetic nerves and CAFs in promoting tumor progression (25), motivating us to investigate these interactions in the CAF-rich context of PDAC.

The roles of fibroblasts and sympathetic nerves in wound healing and injury responses are well established (26, 27). However, their bidirectional interactions with intratumor sympathetic nerves during PDAC progression require further investigation. Fibroblast-derived molecules, such as fibroblast growth factors (FGFs) (28) and fibroblast activation protein (FAP) (29), are typically expressed during nervous system development and can serve as axon guidance cues within developing tumors. Furthermore, a defining characteristic of PSCs, a cell of origin for PDAC CAFs, is storage of esterified retinoids (30). Retinoid signaling plays a critical role in nervous system development and maintenance (31). Similarly, other CAF-derived molecules, such as leukemia inhibitory factor (LIF) (32) and extracellular vesicles containing perineural invasion (PNI)-associated transcripts (PIATs) (33), can directly contribute to neuronal remodeling in PDAC. CAFs also express a variety of axon guidance cues (34), which could contribute to intratumor nerve remodeling and exacerbate tumor-supportive phenotypes in cancer cells. For example, the upregulation of the CAF-derived axon guidance molecule SLIT2 has been linked to neuronal remodeling in PDAC (35). CAF-derived SLIT2 also binds to the ROBO1 receptor on pancreatic cancer cells, activating cortactin (CTTN) and promoting migration (36). A recent study revealed that PDAC-associated CAFs are enriched for neurotropic programs, which may support neurogenesis, neuronal differentiation, and growth (37). Interestingly, these neurotropic programs uniquely overlap with iCAF signatures, but not myCAF or apCAF.

In this study, we combined analysis of human PDAC samples, a pancreas-localized sympathectomy mouse model, and nerve-CAF co-culture systems to investigate the bidirectional crosstalk between

sympathetic nerves and CAFs. Comparative analysis of autonomic innervation in human and murine PDAC revealed a close spatial association between sympathetic nerves and CAFs. Using a non-toxic, pancreas-specific sympathectomy model driven by the dopamine  $\beta$ -hydroxylase (*Dbh*) promoter, we observed significantly reduced tumor growth in female mice. To define the transcriptional impact of sympathetic signaling on CAFs, we performed bulk RNA sequencing using a co-culture system, leveraging primary neonatal superior cervical ganglia (SCG) (38). Sympathetic nerve signaling enhanced CAF activation and ECM remodeling programs, while CAFs reciprocally induced gene expression signatures associated with nerve injury responses in SCGs. Altogether, these findings reveal dynamic, bidirectional interactions between CAFs and sympathetic nerves that contribute to PDAC progression and nominate nerve-stromal crosstalk as a potential therapeutic vulnerability.

## Results:

### Sympathetic innervation is abundant and tied to the survival of PDAC patients

PDAC is known to be influenced by both sympathetic-associated adrenergic (12) and parasympathetic-associated cholinergic (4) signaling. To delineate the autonomic nerve types that physically innervate PDAC, we performed immunofluorescent staining on both human and murine PDAC samples. We observed both autonomic nerve types, parasympathetic, marked by vesicular acetylcholine (VAcHT), and sympathetic, marked by tyrosine hydroxylase (TH), in human PDAC sections (**Figure 1A**, and **Supplemental Figure 1, A-C**). The spatial distribution of parasympathetic and sympathetic nerve bundles showed significant heterogeneity across distinct regions, some demonstrating a prominent VAcHT+ parasympathetic innervation pattern and others primarily representing TH+ sympathetic innervation (**Supplemental Figure 1A, ROI 1 and ROI 2**). Intratumor nerve bundle size and localization also varied significantly (**Supplemental Figure 1B, ROI 1 and ROI 2**). In human tumor-adjacent pancreatic tissue, we observed a few, yet consistent nerve filaments that innervate the exocrine and endocrine areas of the pancreas (**Supplemental Figure 1C, ROI 1 and ROI 2**), similar to murine tumor-adjacent tissues (**Supplemental Figure 1D, ROI 1 and ROI 2**).

To further evaluate the influence of intratumoral nerve-associated gene expression in PDAC, we examined the association between neuronal marker gene expression and overall survival in 208 primary PDAC tumors. This patient data originated from the recently published Oregon Pancreas Tissue Repository (OPTR) cohort (39). High expression of the pan-neuronal gene, beta-tubulin III (*TUBB3*), was associated with poor prognosis (**Figure 1B**). Elevated intratumor expression of the sensory-associated gene, transient receptor

potential vanilloid 1 (*TRPV1*), and the parasympathetic marker *VACHT* (human gene name: *SLC18A3*) showed positive associations with survival. In contrast, elevated *TH* expression correlated with poor prognosis ( $p < 0.05$ ), suggesting differential effects of sensory and parasympathetic versus sympathetic innervation on PDAC survival. We further delineated these neuro-associated gene survival curves by sex and observed similar survival trends in both male and female PDAC patients (**Supplemental Figure 2, A-D**). We also showed that neuro-associated gene expression per PDAC stages remained relatively consistent (**Supplemental Figure 2E**). We further evaluated survival associated with each neuronal marker across patient stage (**Supplemental Figure 2, F-J**). In general, survival trends remained consistent across markers; however, the most pronounced trends were observed in patients with stage 2 disease. We also note that survival associated with high *TH* expression declined rapidly with advancing stages (**Supplemental Figure 2I**). These findings collectively support the hypothesis that sympathetic nerves play an instrumental role in PDAC survival.

### **Murine orthotopic KPC models are innervated by sympathetic nerves**

Sympathetic nerves have been previously observed in KIC (*LSL-Kras*<sup>G12D/+</sup>; *Cdkn2a (Ink4a/Arf)*<sup>lox/lox</sup>; *Pdx1-Cre*) (5) and KPC (*Kras*<sup>LSL-G12D/+</sup>; *Trp53*<sup>LSL-R172H/+</sup>; *Pdx1-Cre*) (40) genetic mouse models of autochthonous pancreatic cancer. The KPC model, which harbors several of the most common human PDAC mutations, progresses through the established developmental stages of PDAC (41) and accurately represents the desmoplastic stroma (42). Here, we evaluated the feasibility of studying sympathetic innervation in the faster-growing orthotopic KPC model. Mice pancreas were intentionally seeded with a low count of KPC (6419c5) (43) cells to allow sufficient time for the nerve and TME landscape to develop. Like in human PDAC, these murine orthotopic KPC tumors were innervated by *VACHT*+ parasympathetic and *TH*+ sympathetic nerves (**Figure 1C**). Compared with human PDAC innervation, intratumor nerve bundles in mice were typically smaller and often contained multiple separate nerve bundles near one another, suggesting decreased spatial heterogeneity in innervation. Sympathetic nerves were predominantly localized along the periphery of murine KPC tumors, with neurites often invading the tumor parenchyma (**Figure 1D**). We also showed similar tumor-adjacent sympathetic innervation of autocrine and paracrine areas in the KPC tumor-adjacent pancreas (**Supplemental Figure 1D**). Overall, these findings demonstrate that slow-growing orthotopic KPC tumors can recapitulate key features of human PDAC sympathetic innervation (5).

### **CAFs surround sympathetic nerve bundles in both human and murine PDAC**

CAFs compose a significant component of the TME of PDAC (16) and can express a variety of axon guidance cues (34–36, 44, 45). To further elucidate the spatial relationship between CAFs and sympathetic nerves within PDAC, we performed immunofluorescent staining, using TH, dopamine beta-hydroxylase (DBH) and alpha-smooth muscle actin (aSMA) markers on both human and murine PDAC samples. Results showed that CAFs closely surrounded sympathetic nerves, and this spatial association was conserved across human and murine PDAC tumors (**Figure 2, A and B** and **Supplemental Figure 1, E and F**). This suggests the potential positive affinity and reciprocal signaling between tumor-innervating sympathetic nerves and CAFs.

### **Generating a pancreas-localized, sympathetic-specific genetic ablation murine model**

We sought to disrupt sympathetic innervation in PDAC tumors in vivo to interrogate sympathetic-specific contributions. Current murine sympathectomy models have yielded contradictory insights, and further evidence is required to definitively determine the role of sympathetic nerves in PDAC. Two previous studies blocked sympathetic activity via systemic administration of beta-blockers and reported reduced PDAC cell proliferation and improved survival in tumor-bearing mice (12, 46). Other studies have selectively ablated adrenergic and dopaminergic neurons by administering the neurotoxic chemical, 6-hydroxydopamine (6-OHDA), which induces oxidative stress and, consequently, neuronal death. One study showed that orthotopically implanted pancreatic tumors were smaller after denervation (14), whereas another study demonstrated that 6-OHDA treatment led to larger pancreatic tumors and enhanced metastasis (5). To clarify these differing results, we generated a non-toxic, pancreas-specific genetic sympathectomy model that can serve as a powerful tool to delineate the specific influences of sympathetic nerves on murine PDAC tumor growth and the TME composition.

To selectively target sympathetic innervation, we identified DBH as a sympathetic-specific marker, offering greater specificity than TH, given its downstream role in converting dopamine to norepinephrine, the primary sympathetic neurotransmitter (47). Immunofluorescent staining of ex vivo superior cervical ganglia (SCG) explant neurite outgrowth served as a robust model of sympathetic nerves. We showed consistent DBH expression throughout the extension of the axons, co-stained by the neurofilament-medium (NF-m) pan-neuronal marker (**Figure 3A**). Furthermore, we observed consistent DBH staining in both human and mouse PDAC innervation (**Supplemental Figure 1, E and F**). To achieve targeted sympathetic denervation, we generated an inducible chemo-genetic ablation murine model by crossing a heterozygous *Dbh-Cre* (B6.Cg-*Dbh*<sup>tm3.2(cre)Pjen</sup>/J) mouse with a homozygous *Rosa26-iDTR* (C57BL/6-*Gt(ROSA)26Sor*<sup>tm1(HBEGF)Awai</sup>/J) mouse line (**Figure 3B**). The resulting cross produced half of the offspring expressing the diphtheria toxin receptor (DTR),

specifically in sympathetic neurons, rendering them susceptible to ablation upon exposure to diphtheria toxin (DT). The remaining half of the offspring served as controls, lacking Cre and therefore the DTR expression and thus not susceptible to DT-induced ablation. With this model, all mice received several intra-pancreatic DT injections to ensure consistency across cohorts and to control for off-target effects of DT or potential injection-related inflammation.

Intra-pancreatic DT treatment demonstrated a robust and consistent reduction of DBH expression in cleared and stained healthy pancreas tissues (**Figure 3C**). We observed a consistent reduction in DBH staining across low, mid, and high DT doses. Both male and female cohorts were analyzed, and tissues were evaluated one month after ablation to ensure that the ablations remained consistent for the duration of our slow-growing orthotopic tumor model.

Next, we applied our validated inducible denervation method to study the effects of sympathetic nerve ablation in our syngeneic orthotopic KPC tumor model. We administered four intra-pancreatic injections of DT, immediately followed by a KPC (6419c5) cell injection (**Figure 4A**). Simultaneous administration was key to reducing additional stress and off-target effects and allowing the KPC tumors to initiate and progress in a sympathetically depleted pancreas. To confirm the efficacy of these intra-pancreatic DT administrations, we performed immunofluorescent staining for TH expression in tumor-adjacent pancreata (**Figure 4B**), and normalized quantification revealed a significant reduction in sympathetic nerve density in both male and female ablated cohorts (**Figure 4C**). In addition to validating DBH depletion in the tumor-adjacent pancreas, we demonstrated that there was no change in TH expression in the colons, lungs, and hearts of mice in either cohort of our model (**Supplemental Figure 3, A-C**). We also showed representative images of male and female intratumor innervation in control and ablated animals (**Supplemental Figure 3D**). Furthermore, systemic health metrics, including body weight, inflammation-induced spleen changes, and glucose levels, were assessed to ensure that sympathetic ablation did not cause significant physiological distress (**Supplemental Figure 3, E-H**). Overall, we validated that this approach led to precise, inducible elimination of sympathetic nerves.

### **Pancreas-specific sympathectomy reduced tumor size in female mice**

Despite effective pancreatic sympathectomy, initial analysis of tumor size across all samples did not show significant differences between control and denervated groups (**Figure 4D**). However, when stratified by sex, a distinct pattern emerged: male tumor weights remained unchanged (**Figure 4E**), whereas female tumor weights and sizes were significantly reduced by sympathectomy (**Figure 4, F-G**). Further analysis revealed a

positive correlation between nerve density and tumor weight in females, suggesting a potential role for sympathetic signaling in female-specific tumor progression (**Figure 4H**). These results indicated that sympathetic denervation selectively impacted tumor growth in female but not male mice in our KPC model, suggesting a potential sex-dependent influence of adrenergic signaling on PDAC progression (**Supplemental Figure 3I**).

Given our observed differences in tumor size and the known role of adrenergic signaling in promoting PDAC cell proliferation (12), we evaluated the proliferative effects of sympathetic nerve stimulation. Using the primary SCG explant model, we assessed the impact of potential paracrine adrenergic signaling on murine KPC cancer cells and CAFs by measuring proliferation (**Figure 4I**). SCG-conditioned media significantly enhanced the proliferation of KPC cell line 6419c5 cells, the same line used in our orthotopic model (**Figure 4J**). To investigate the effect of SCG paracrine signaling on CAF proliferation, we used the mPSC1 (PSC) cell line. This PSC cell line was derived from murine pancreatic tissue, becomes activated upon plastic adherence, and shows significant heterogeneity (20, 30), thus providing a biologically relevant framework for in vitro CAF studies. Our results demonstrated that SCG-conditioned media also significantly enhanced PSC cell proliferation (**Figure 4K**). These findings suggest that sympathetic nerves simultaneously promote the proliferation of tumor cells and CAFs, which may explain the increased tumor growth observed in control mice compared with sympathectomized mice.

### **SCG signaling activates CAF genes associated with poor patient outcomes**

Although CAFs regulate a variety of axon guidance cues, including Slit2 (35, 36), Sema3a (44), Sema3d (45), Netrin-1 (48), and Netrin-G1 (21), it remains unclear whether CAFs actively respond to sympathetic signaling. Using an indirect SCG explant co-culture system with activated PSCs, we investigated the transcriptional effect of sympathetic signaling on activated PSCs (**Figure 5**). We separated SCG explants from PSCs using trans-well inserts, co-cultured for 70 hours (**Figure 5A**), and performed bulk RNA sequencing to identify differentially expressed genes in PSCs upon exposure to sympathetic-derived signaling. PSCs exposed to SCG-derived adrenergic signaling significantly upregulated 35 protein-coding genes ( $\log_2$  fold change  $\geq 0.5$ , adjusted  $p \leq 0.05$ ) (**Figure 5B** and **Supplemental Figure 4, A-C**). Upon initial evaluation, several upregulated genes, including *GAS1*, *GABRE*, *LAMA4*, *MMD*, *OSMR*, *PLOD2*, and *ST4GAL1*, are associated with poorer prognosis in the human OPTR PDAC cohort (**Supplemental Figure 4D**).

## SCG signaling drives CAF activation and extracellular matrix (ECM) remodeling

To further characterize PSC transcriptional shifts induced by sympathetic signaling, we performed gene set enrichment analysis (GSEA). A query of several upregulated pathways revealed a strong association with CAF activation and ECM remodeling (**Figure 5C**). EMT-related genes were strongly enriched, with the top 30 genes including *Fap*, *Fgf2*, *Cxcl5*, and *Wnt5a* (**Figure 5D**). Functionally, we showed that SCG-conditioned media increased CAF invasion (**Figure 5E**). We also observed significant enrichment of IL6/JAK/STAT3 signaling (**Figure 5F**), consistent with a shift toward an iCAF phenotype. Using the sympathetic ablation model, we evaluated the iCAF and myCAF states in response to sympathetic input. We showed that the tumors derived in female mice, which showed a significant reduction in tumor size in response to sympathectomy, had a 6% lower iCAF to myCAF ratio, whereas male-derived tumors had approximately the same ratios (**Figure 5, G and H** and **Supplemental Figure 5, A-D**). Additionally, PSCs treated with SCG media significantly upregulated iCAF-associated cytokines (**Supplemental Figure 5, E and F**).

We also identified strong enrichment for ECM remodeling pathways (**Figure 5C** and **Figure 5I**), suggesting that sympathetic nerves could influence CAF function and ECM deposition, which have previously been shown to support cancer progression and metastasis (49). Furthermore, genes enriched in extracellular structure organization revealed a broad set associated with matrix deposition, degradation, and reorganization. We evaluated ECM in the in vivo sympathetic ablation model and found a subtle, yet non-significant decrease in ECM density in ablated tumors of female mice (**Figure 5J** and **Supplemental Figure 5, G-I**). Collagen fiber alignment, coherency, and orientation were unchanged between control and ablated tumors (**Supplemental Figure 5, J and K**). When treating PSCs with SCG media in vitro, PSCs were significantly less adherent to Collagen I as compared to fibronectin, collagen IV, laminin I, and fibrinogen (**Figure 5K**), which supports the findings of SCG-induced ECM remodeling in PSCs and also the iCAF phenotypic shift.

## PSC-derived SEMA3C expression in response to sympathetic signaling enhances PDAC EMT

In addition to CAF-related pathways, we identified six genes (18% of the total significantly upregulated genes) associated with cell-cell attachment and nerve-related signaling (**Supplemental Figure 6A**). These genes include: *Cck*, *Sema3c*, *Gria4*, *Slc1a3*, *Gas1*, and *Pcdh10*. Although CAFs have been shown to inherently express neuro-associated genes (28, 34), our results suggest that sympathetic signaling may amplify this neuro-associated gene expression in CAFs, potentially driving a feed-forward loop of nerve-stroma crosstalk within the TME that influences PDAC tumors. The axon guidance cue, semaphorin 3c (SEMA3C), emerged as a key candidate, as high intratumor SEMA3C expression was strongly associated with poor survival in female patients with PDAC (**Figure 6A** and **Supplemental Figure 6B**). We also noted that the expression of the canonical receptors for SEMA3C, NRP1, and NRP2 was associated with poor survival in PDAC patients (**Figure 6B** and **Supplemental Figure 6C**). We validated that PSC cells significantly

upregulated SEMA3C in both indirect (+SCG media) and direct (+SCG direct) cocultures with SCGs (**Figure 5, C and D**). We also found that NRP1 is significantly upregulated in murine KPC tumor tissue, as compared to the tumor-adjacent pancreas (**Supplemental Figure 6D**), and that NRP1 is expressed in both well-differentiated and poorly differentiated regions of these KPC tumors (**Supplemental Figure 6E**). We further observed that NRP1 is expressed by both cancer cells and fibroblasts in murine KPC tumors (**Supplemental Figure 6E**) and human PDAC (**Figure 6E**).

Previous literature has identified SEMA3C as a contributor to EMT in pancreatic (50), prostate (51), and breast cancers (52); therefore, we further evaluated ECM-associated shifts. The treatment with recombinant SEMA3C resulted in an increase in PSC proliferation (**Supplemental Figure 6F**) and a significant increase in KPC cell invasion (**Figure 6F**). We also confirmed that both SNAIL/SLUG and VIMENTIN expression were increased in both murine KPC (**Figure 6, G and H**) and human Panc1 (**Figure 6, I and J**) cells upon treatment with recombinant SEMA3C. We note that recombinant mouse SEMA3C also altered PSC cytokine profiles toward an iCAF-like state, recapitulating the effects of sympathetic neuron-derived SCG media (**Supplemental Figure 5, E and F**).

### **KPC cells and activated fibroblasts enhance axon outgrowth**

Neuronal cell bodies are located outside the target organ, posing challenges for capturing transcriptional changes in nerves in response to cancer growth and stromal changes. A recent study used retrograde tracing to sequence pancreatic tumor-innervating nerves, identifying CAFs as potential partners in the PDAC TME (14). To model sympathetic axon outgrowth and transcriptomic changes that are induced by CAFs, we leveraged our SCG explant trans-well co-culture model with activated PSCs. Our SCG explant model uniquely preserves several components of the ganglia structure and microenvironment, including glial cells, which play an essential role in neuronal maintenance and function. SCG explants were co-cultured in trans-wells with control fibroblast (mouse embryonic fibroblasts (MEFs), NIH/3T3 cells), activated PSC (mPSC1), or KPC (6419c5) cells (**Figure 7A**). Axon extension was captured using phase-contrast microscopy over a 24-hour period to quantify neuronal outgrowth (**Figure 7B**). Neurite extensions emanating from each individual SCG explant were traced and averaged across co-culture systems. As expected, SCG explants co-cultured with our positive control, KPC cells, which secrete a variety of neural growth factors, significantly increased axon outgrowth (**Figure 7C**). SCG explants co-cultured with activated MEFs and PSCs resulted in only a marginal increase in axon extension. We also showed increased axon outgrowth rates in SCG explants cocultured directly and indirectly with activated PSCs (**Supplemental Figure 7, A and B**) and preferential

growth toward PSCs within a Matrigel dome (**Supplemental Figure 7, C and D**). These observations suggest that fibroblasts might exert more subtle phenotypic effects on sympathetic nerve outgrowth.

### **Activated PSCs induce injury response in SCG explants**

To investigate the impacts of MEFs versus activated PSCs on SCG transcription, we sequenced SCG explants following co-culture. We identified several protein-coding genes that distinctly shifted under culturing conditions, with MEFs inducing fewer transcriptional changes than activated PSCs (**Figure 8A** and **Supplemental Figure 7, E and F**). GSEA revealed significant enrichment in several categories previously shown to be related to nerve injury responses, such as cell cycle (53), immune response (54), metabolism (55), neuron plasticity (56), and select signaling pathways associated with injury response (57) in the setting of PSC co-culture (**Figure 8B**). We also note that MYC signaling (58), MTORC1 (59), IL-6/JAK/STAT3 signaling (60), and EMT (61) were also enriched and are associated with peripheral nerve injury response (**Supplemental Figure 7G**). These results suggest that exposure to PSC-derived CAFs further exacerbates the transcriptional response to sympathetic nerve injury.

### **Activated PSCs reprogram sympathetic nerve transcriptional programs toward a sustained injury response**

Beyond shifts in injury-associated transcription, we observed that activated PSCs induced greater changes in gene expression than MEFs, with only 28 protein-coding genes (7.8%) shared between conditions (**Figure 8C**). In contrast, 280 genes (78.2%) were significantly upregulated in response to activated PSCs, indicating a more profound impact of activated PSCs on SCG transcriptional programs.

Upon examination of the overlapping genes enhanced by both fibroblast cell lines, we identified several genes for nerve injury as well as ligands, receptors, and transcription factors that may influence sympathetic neuron phenotypes. Of the 28 overlapping SCG genes enhanced by both PSCs and MEFs, *Ccr1*, *Ntm*, and *Sema3a* stood out as genes associated with nerve injury, while several ligands, such as *Ccl6*, *Pfa*, *Sema3a*, and *Mmp12*, and receptors, such as *Cyp1a1* and *Il4ra*, were upregulated (**Figure 8D** and **Supplemental Figure 7H**). Upon closer examination of the 280 genes uniquely upregulated when SCGs were co-cultured with PSCs, we identified several additional genes that may contribute to a sustained injury response in

sympathetic neurons. Some of the nerve injury-associated genes included *Ifih1*, *Cxcl10*, *Stat1*, and *Trim21* (Figure 8F). Furthermore, upregulated ligands included *Cxcl3*, *Cxcl10*, and *Ccl9*, while upregulated receptors include *Irh1*, *Clec4n*, and *Il1rap*. Differentiating these unique gene changes provides insights into the general transcriptional shifts induced by activated fibroblasts and the pancreatic-specific CAF-induced shifts. We also highlight that each receptor or ligand has binding potentials and that several genes encoding proteins, such as *Ccl6* (62), *Pf4* (63), *Sema3a* (44), *Cxcl3* (64), *Cxcl10* (65), and *Ccl9* (66), have been shown to have broader tumor-supportive roles in PDAC.

## Discussion:

Sympathetic influences are increasingly recognized to have roles in tumor initiation, progression, and recurrence in PDAC (10, 12, 46, 48). To overcome the limitations of current mouse models of sympathetic innervation in PDAC, we developed a novel genetic sympathectomy KPC model to elucidate the direct contributions of sympathetic nerves to PDAC progression and to changes in the TME, particularly CAFs. We further identified specific transcriptional programs leveraging ganglia explant co-culture systems, in which we observed that adrenergic signaling induced CAF activation and ECM remodeling, while CAF signaling exacerbated sympathetic injury response. Our results provide further understanding of the specific reciprocal interactions between sympathetic nerves and CAFs in PDAC tumors.

Previous chemical sympathectomy strategies used in PDAC have yielded seemingly contradictory results and the potential for off target effects (5, 14, 46, 67, 68). Systemic inhibition of sympathetic signaling using  $\beta$ -blockers has been shown to reduce PDAC proliferation and improve survival (12, 46). In contrast, studies using chemical sympathectomy via 6-OHDA have reported divergent outcomes: one study showed decreased tumor sizes (14), whereas another observed larger tumors and increased metastasis (5). Several biological factors may account for these opposing findings. Unlike  $\beta$ -blockade, which functionally inhibits adrenergic signaling, 6-OHDA induces neuronal death through dopamine and norepinephrine transporter-mediated uptake and ROS-driven mitochondrial injury, introducing oxidative stress that may also alter the pancreatic microenvironment. Systemic administration or diffusion of the chemical may also affect off target organs as well as differentially influencing stromal remodeling, immune composition, and tumor-nerve dynamics, contributing to disparate outcomes across studies. In addition, the timing of denervation, whether performed during early or late-stage tumor evolution or at differing ages and therefore interacting with developmental or hormonal differences, may further contribute to variable outcomes. These complexities motivated our development of a non-toxic, pancreas-localized chemo-genetic sympathectomy model, which

enabled us to define the direct role of sympathetic nerves in PDAC independent of systemic or ROS-related effects.

Our novel chemo-genetic sympathectomy model is non-toxic, sympathetic-specific, and pancreas-localized (**Figure 3** and **Figure 4**). Previous studies have produced a systemic *Th* Cre-inducible; DTR-fl/stop/fl DT-inducible ablation, showing that this model's effects cannot cross the blood-brain barrier and ablating only peripheral nerves (69). Although considered a robust sympathetic marker, TH converts upstream L-tyrosine into L-DOPA. Therefore, a limitation of this method is that it broadly targets all dopaminergic neurons and dopamine-expressing cells, including pancreatic alpha-cells. To address sympathetic specificity, we targeted DBH, which lies downstream of TH and converts dopamine to norepinephrine. To achieve localized effects, we optimized a protocol, ultimately arriving at multiple low-volume intra-pancreatic injections. In addition to validating the reduction in sympathetic innervation using 3D clearing and imaging techniques, we confirmed that our ablation model was non-toxic by observing grossly normal behavior and health measures after ablation (**Supplemental Figure 3**). Despite the overtly efficient and specific ablation of sympathetic nerves throughout the PDAC tumors and tumor adjacent pancreas, a small portion of TH-staining nerves remained, potentially representing remnants of non-functional neurons. Further functional studies would be required to determine the extent of the activity of the remaining sympathetic signaling. Altogether, this non-toxic model successfully establishes a reliable, sympathetic-specific approach, introducing a novel tool to explore the local impact of sympathetic innervation in PDAC and other cancer models.

To investigate the specific influence of sympathetic nerves on PDAC, we utilized our sympathectomy method in a slow-growing KPC orthotopic tumor model. In vivo sympathetic nerve studies have primarily been performed using genetically engineered mouse models (GEMMs). We applied our sympathectomy model to orthotopic KPC tumors, characterized by rapid growth, an intact immune system, dense desmoplastic stroma, and limited responsiveness to administered treatments (70). We observed significantly smaller KPC tumor sizes in sympathectomized females, whereas male mice showed no difference (**Figure 4**). We note that the 6419c5 KPC cells were originally derived from female mice; therefore, there is minimal concern about cross-reactivity in these experiments. We note that autonomic regulation and downstream physiological effects can differ between males and females, which may contribute to the differential tumor susceptibility following sympathetic ablation.

Overall, our in vivo ablation results suggesting intriguing links between biological sex and sympathetic signaling in PDAC, raise questions about how sex hormones interact with sympathetic nerves in the disease. Prior studies have shown that males exhibit higher sympathetic activity in certain peripheral tissues, including adipose tissue, influencing metabolic and stress-response pathways (71). Further studies have shown that males tend to have higher sympathetic activity, while females typically have higher parasympathetic activity, and that

there are measurable sex differences in peripheral nerve injury responses (72). Sympathetic innervation also shapes immune function in a sex-dependent manner (73), and sex hormones further regulate immune and inflammatory signaling, including pain-related pathways (74). Females typically display a more pronounced inflammatory response, influenced in part by reduced androgen levels (75). Notably, a recent study reported that higher peri-tumoral  $\beta$ 2-adrenergic receptor staining was associated with significantly poorer survival, specifically in female PDAC patients, suggesting a sex-specific susceptibility in the context of sympathetic signaling (10). These converging findings underscore the need for future larger-scale studies to rigorously define sex as a biological variable in PDAC–neuron interactions. Leveraging more sensitive tools, such as the chemo-genetic ablation model we generated, could provide critical insights into overall and distinct shifts in cellular composition, signaling pathways, and spatial interactions within the TME.

We demonstrated that CAFs closely surround sympathetic nerves both in murine and human PDAC (**Figure 2**). To better understand the interactions between sympathetic nerves and CAFs, we used SCG explants to investigate bidirectional paracrine signaling between these cell types. Although SCGs do not directly innervate the pancreas, we selected SCGs for our in vitro modeling studies because they are composed predominantly of postganglionic sympathetic neurons and provide a consistent, well-characterized source of adrenergic input by releasing norepinephrine (76) and some NPY. No cholinergic characteristics were previously observed in these ganglia (77). It is noteworthy that celiac ganglia (CGs) which more directly innervate the pancreas, release a wider range of neurotransmitters, including norepinephrine, NPY, calcitonin gene-related peptide (CGRP), and nitric oxide (NO) (78). However, recent evidence suggests that CGs feature both noradrenergic and cholinergic characteristics by expressing somatostatin (SST) and vasoactive intestinal peptide (VIP), as neurons extending from these ganglia are specialized for gut regulation (77).

Co-culturing activated pancreas-derived fibroblasts with primary SCG explants revealed changes in the transcriptional programs of the activated PSCs that may directly contribute to tumor progression (**Figure 5** and **Figure 6**). Because CAF subtype specification is shaped by both cell-of-origin and microenvironmental cues, our results suggest that sympathetic nerves serve as niche signals that influence fibroblast activation and fate. PSCs, which already exhibit a partial neuronal-like transcriptional program, may be particularly receptive to sympathetic neural cues, enabling neural signaling to promote iCAF differentiation and ECM remodeling, both key features of tumor progression. We found that sympathetic signaling activates these pancreas-derived CAFs through IL6/JAK/STAT3, Notch, TGF- $\beta$ , and TNF $\alpha$  pathways. We also observed strong enrichment of ECM remodeling programs, a hallmark of CAF-mediated support of PDAC progression (49). Several of the upregulated genes are associated with poor survival of patients with PDAC. Importantly, multiple sympathetic signaling-induced genes encode ligands released into the TME, most notably the axon guidance cue, *Sema3c*, which bind to receptors such as NRP1 and NRP2, which we show are associated with poor PDAC outcomes. SEMA3C upregulation is known to drive EMT in prostate cancer (51), and in PDAC it is instrumental in tumor

growth and metastasis, enhancing proliferation and suppressing apoptosis through ERK1/2 activation (79). Together, these findings highlight how sympathetic signaling directly reprograms pancreas-derived CAFs toward tumor-supportive functions, reinforcing a feedforward loop within the TME. Future work could spatially resolve these receptor-ligand interactions between CAFs and sympathetic nerves in vivo and expand understanding of other TME interactions such as, immune infiltration.

Our data supported that CAFs can substantially alter SCG transcription and contribute to nerve injury response (**Figure 8**). Although nerve bodies typically do not divide and thus would not be expected to express cell cycle genes, previous studies suggest that upregulation of cell cycle, immune response, metabolism, and neuron plasticity genes are often linked to peripheral nerve injury (53–56). It is important to note that plated SCG explants are intrinsically in an injury-response state due to their displacement from their native environment (80). However, we ensured even plating in all conditions and reduced stress on neurons by keeping them in their explant form. Our transcriptional observed shift suggests that CAFs may further contribute to neuronal stress and injury responses in PDAC. We also noted that CAFs derived from the pancreas (PSCs) exhibited a more pronounced transcriptional effect than the control fibroblasts, MEFs. Upon closer examination, we also found that the transcriptional influences are markedly different, with only 7.8% overlap between SCG explants co-cultured with PSCs versus MEFs. These findings pose interesting questions about whether pancreas-derived CAFs induce a stronger nerve injury response in sympathetic nerves, facilitating their activation and reorganization during PDAC growth. A limitation of our system is its focus on paracrine crosstalk rather than direct cell-to-cell interactions, which may underestimate the extent of bidirectional transcriptional regulation. Single-cell studies could help further distinguish differences in paracrine and physical interactions between SCGs and CAFs, offering deeper insight into their dynamic interplay in PDAC.

In summary, our study highlights neuro-associated survival trends in patients with PDAC and introduces a novel sympathectomy murine model, which could serve as a powerful tool for investigating sympathetic innervation across diverse tumor models. By delineating the intricate interactions between sympathetic nerves and CAFs, we uncovered potential drivers that mediate the bidirectional communication. This work provides a framework for elucidating a deeper understanding of nerve-TME dynamics in PDAC and their contributions to tumor progression, paving the way for more effective, targeted therapeutic strategies.

## Methods:

*Sex as a biological variable.* Generated survival curves represented both male and female patients. Experiments examined male and female animals, and sex-dimorphic effects were reported and discussed.

*Survival curve generation.* Using survival data from 208 de-identified patients diagnosed with PDAC between 2004 and 2020 (39). Kaplan-Meier plots and statistics were derived using R version 3.6.3 and the “survival” package version 3.3.1. A single primary PDAC tumor sample underwent bulk RNA sequencing. Tumor high vs. low expression of the selected gene was stratified using a threshold that maximized the log-rank p-value, and the results were reported using the log-rank test. Each stratum contained at least 10 patients, and significance was assessed using a p-value < 0.05. Benjamini-Hochberg FDR correction was performed to calculate adjusted p-values.

*Murine breeding pairs for SCG dissections.* Wild-type C57BL/6J (The Jackson Laboratory; 000664) female (aged 2 to 8 months) underwent 3 to 5 rounds of breeding to male wild-type mice (aged 2 to 12 months). Post-natal day 1 to day 4 mice were euthanized in accordance with our IACUC protocol and utilized for SCG co-culture experiments.

*Generation of sympathectomy genetic cross.* Homozygous C57BL/6-*Gt(ROSA)26Sor<sup>tm1(HBEGF)Awai</sup>/J* (The Jackson Laboratory; 007900) mice were crossed with heterozygous B6.Cg-*Dbh<sup>tm3.2(cre)Pjen</sup>/J* (The Jackson Laboratory; 033951) mice generating *Rosa26-iDTR/Dbh-Cre* and *Rosa26-iDTR/Dbh-WT* offspring for. Male and female mice were used, and surgeries were conducted between 14 and 16 weeks of age and tumor growth ranged between 28 and 32 days.

*Cell culture.* Murine control mouse embryonic fibroblasts (NIH/3T3 ATCC CRL-1658), immortalized murine PSC cell line (mPSC1 (20)) and 6419c5 cells (CVCL\_YM21, provided by Dr. Stanger, Philadelphia) were cultured in Dulbecco's modified Eagle's medium (DMEM; Gibco; 11965-092) with 10% fetal bovine serum (FBS; Gibco; Thermo Fisher Scientific, Inc.) and 1% penicillin/streptomycin. Cells were maintained at 37 °C in a humidified incubator containing 5% CO<sub>2</sub> and split at 80% confluence for no more than 25-30 passages. Cell lines were routinely tested for mycoplasma.

*Diphtheria toxin inducible sympathectomy.* To validate the sympathectomy using diphtheria toxin (DT; Caymen Chemicals; 19657), we initially performed systemic sympathectomies, delivering 500 ng DT via intraperitoneal injection (n = 3 *Rosa26-iDTR/Dbh-WT*; n = 3 *Rosa26-iDTR/Dbh-Cre*). Healthy pancreata were collected and fixed two weeks later. For validation of pancreas-specific sympathectomy, we injected 20 µl of DT into four sites along the pancreas. We tested three DT total concentrations, including low 100 ng (n = 1 *Rosa26-iDTR/Dbh-WT*, n = 1 *Rosa26-iDTR/Dbh-Cre*), mid 250 ng (n = 2 *iDTR/Dbh-WT*, Cre+ n = 2 *Rosa26-iDTR/Dbh-*

Cre), and 500 ng (n = 2 *Rosa26-iDTR/Dbh*-WT, n = 2 *Rosa26-iDTR/Dbh*-Cre). Pancreata were collected and fixed 4 weeks post-DT injections. Both male and female mice were used for these validations, and ablations were confirmed by 3D immunofluorescent staining.

*Orthotopic PDAC transplant/allograft model.* Animals were anesthetized, and four intra-pancreatic DT injections (4 X 20  $\mu$ l DT, totaling 500ng) were delivered. Next,  $2.5 \times 10^3$  6419c5 cells in 50% 1X Phosphate-buffered saline (PBS) and 50% Matrigel Matrix (Corning; 356231) were injected into the pancreas. Between days 28 and 32 post-transplantation, animals were euthanized and perfused with 1X PBS and then with 4% paraformaldehyde (PFA). Tumors, tumor-adjacent pancreas, liver, lungs, spleen, and colon were carefully excised, weighed, and fixed overnight in 4% PFA and transferred to 70% ethanol at 4 °C for storage.

*Superior cervical ganglia dissections and co-cultures.* SCGs were extracted as described by Jackson & Tourtellotte (81). Under a dissecting microscope, SCGs were located medial to the bilateral carotid arteries, identifiable by their translucent color and large nerve branch on the superior portion of the ganglia. Using fine forceps, both SCG were carefully extracted and placed in cold 1X Hanks Balanced Salt Solution (HBSS; Gibco; 14170-112). Excess tissue was removed from the ganglia. SCG were dissociated with collagenase type 2 (Worthington Biomedical; LS004174) for 30-35 min at 37 °C and inverted every 10 minutes, then washed in Dulbecco's modified Eagle's medium (DMEM; Gibco; 11965-092) containing 10% fetal bovine serum (FBS; Gibco; Thermo Fisher Scientific, Inc.), 1% penicillin/streptomycin, and 5ng nerve growth factor (NGF 2.5S; Gibco; 2402212). Using a fiber-polished glass pipette, SCG were triturated until the desired explant size was reached. The SCG explants were carefully plated into wells coated overnight at 37 °C with a mixture of 100  $\mu$ g/ml Poly-D-lysine hydrobromide (MP Biomedicals; 0210269480) and 10  $\mu$ g/ml Laminin (Thermo Scientific; 23017015). Thirty minutes prior to plating SCG explants, wells were washed 1X with sterile water and dried at 37 °C. SCG explants were either cultured directly together on the same surface or separated by an insert.

*SCG explant cultures for proliferation assays.* Between 10-20 explants were plated in a coated 24-well plate and allowed to grow for about 70 hours. SCG explant-conditioned media was transferred to proliferation assays.

*Axon outgrowth co-culture.* Between 4 and 6 explants were plated per 6-well plate.  $10.0 \times 10^3$  immortalized cells were added simultaneously to cell culture inserts (Falcon; 353090) and incubated for 70 hours. Phase-contrast imaging captured axon outgrowth.

*RNA-seq co-culture.* Between 8-13 explants were plated in coated 6-well plates and grown with  $10.0 \times 10^3$  immortalized cells on inserts (Falcon; 353090) for about 70 hours. RNA was isolated using the RNeasy Kit (Qiagen; 74104).

*In vitro cell staining.* Cells were fixed with 4% PFA, washed 3X with PBS, and blocked in 8% bovine serum albumin (BSA). Cells were incubated overnight with primary antibodies (**Supplemental Table 1**) in 1% BSA at 4 °C, then washed three times in 1X PBS for 5 minutes each. Secondary Alexa Fluor-conjugated antibodies in 1% BSA were added in 1% BSA for 2 hours (**Supplemental Table 1**) at room temperature. Cells were washed 3X for 5 minutes in 1X PBS and stained with DAPI (Thermo Scientific; 62248, lot: XL3789541) at 1:1000. Cells were imaged in fresh 1X PBS.

*Immunofluorescent staining of FFPE tissue sections.* Sectioned FFPE tissues were deparaffinized and rehydrated through a xylene and ethanol series, finishing with 1X PBS. Upon antigen retrieval with Antigen unmasking solution (Vector Laboratories; H-3300) in a high-pressure cooker for 15 minutes, sections were washed and blocked for 30 minutes in 8% BSA at room temperature. Unconjugated primary antibodies (**Supplemental Table 1**) were applied in 1% BSA and incubated overnight at 4 °C. Upon 3X 5-minute 1X PBS washes, secondary antibodies (**Supplemental Table 1**) diluted in 1% BSA were added for 2 hours. Sections were washed, quenched using the TrueVIEW reagent (Vector Laboratories; NC202386) and stained with DAPI (Thermo Scientific; 62248, lot: XL3789541) 1:000. Sections were washed and then mounted using ProLong Gold antifade reagent (Life Technologies Corporation; P36930).

*IDISCO.* IDISCO was performed on sections of KPC orthotopic tumors, as described by Renier, N. et al. 2014 (82), and the associated protocol (<https://idisco.info/>). Fixed tumors were sectioned into 2-3 mm slices. Samples first underwent methanol pretreatment, delipidated in dichloromethane (DCM) (Sigma Aldrich; 270997-12X100ML), bleaching in 5% H<sub>2</sub>O<sub>2</sub> in methanol, rehydrated in a decreasing concentration methanol series, and then washed with the PTx.2 mix (10x PBS and TritonX-100 (Sigma Aldrich; X100-500ML)). Next, samples were permeabilized for 2 days (PTx.2, glycine (Sigma Aldrich; G7126-500G) and dimethyl sulfoxide) and blocked (PTx.2, donkey serum (Jackson Immuno Research Labs; 017-000-12) and dimethyl sulfoxide). Samples were washed with PTwH solution (10X PBS, Tween-20 (Sigma Aldrich; P9416-100ML), and heparin (Sigma Aldrich; H3393-50KU), and incubated with the primary antibody (**Supplemental Table 1**) for 4 days. Following additional washes in PTwH solution, tissues were incubated for 4 days with secondary antibodies (**Supplemental Table 1**). Upon PTwH washes, samples underwent a methanol dehydration series. Lastly, samples were transferred to DiBenzyl Ether (DBE) (Sigma Aldrich; 108014-1KG) and mounted in DBE on two-sided 1.5 µm coverslip chambers constructed from a thin silicone sheet with a round cutout, secured using silicone glue.

*EZ Clear.* The EZ Clear protocol was performed on tumor-adjacent pancreata and 2-3 mm tumor sections, as described by Hsu, C.H. et al. 2022 (83). Samples were rehydrated in 1X PBS and delipidated in a 50% Tetrahydrofuran (THF) (Millipore-Sigma; 186562) and 50% water mixture for 2 days, then washed with 1X PBS and blocked (1X PBS, Triton X-100, donkey serum, and sodium azide (Millipore-Sigma; S2002) for two more days. Primary antibodies (**Supplemental Table 1**) were incubated in blocking solution for 3 days. Samples were washed with 1X PBS, and the secondary antibody (**Supplemental Table 1**) was added and incubated for 3 days. Tissues were then washed with 1X PBS, and EZ Clear solution was added ((sodium phosphate, urea (Millipore-Sigma; U5378), sodium azide (Millipore-Sigma; S2002), and nycodenz (Accurate Chemical & Scientific; 100334-594)) overnight. Fresh EZ Clear solution was used to mount tissues between two-sided 1.5 µm coverslip chambers constructed from a thin silicone sheet with a round cutout, secured with silicone glue.

*Picro sirius red staining.* Collagen fibers were visualized using the Picro Sirius Red Stain Kit (Abcam; ab150681). FFPE sections were deparaffinized and rehydrated through the following graded series: 3 X 5 minutes in 100% xylene, 2 X 2 minutes in 100%, 2 X 2 minutes in 95%, 1 X 2 minutes in 70% ethanol, and rinsed in distilled water. Sections were incubated for 2 hours with 150 µL of Picro Sirius Red solution at room temperature on a rocker, and then 200 µL of the acetic acid solution was applied twice in 4-minute incubations. Sections were then dehydrated in 95%, then 100% ethanol, and cleared in 100% xylene (4 minutes each). Coverslips were mounted using resin-based mounting medium (Permount, EMS; 17986-01).

*Confocal microscope.* Cleared tissues were imaged using an inverted laser-scanning confocal microscope with Airyscan.2 (Carl Zeiss, LSM 980) and a 10X air objective. Tiles were stitched and quantification was completed using the Zen microscopy software.

*ApoTome3.* Stained FFPE tissues and cells were imaged using the ApoTome3 grid-based optical sectioning microscope (Carl Zeiss). 10X and 20X air objectives were used. Zen microscopy software automated tile fusion and quantification.

*AxioScan slide scanner.* Whole-slide scanning was performed using the Zeiss AxioScan 7 Slide scanner. The automatic scanner acquired 20X tiled images of tissue sections. Automated tile processing fused images.

*Cytation 5.* Explant axon outgrowth was imaged using digital phase-contrast was acquired using the BioTek Cytation 5. The microscope incubator was set at 37 °C, and automated exposure and focusing were used. Outgrowth was quantified using ImageJ tracing and quantification (8+ random, equally distributed locations).

*IncuCyte live-cell analysis systems.* For wound-healing assays, we used the IncuCyte system from Sartorius wound-healing program, 10X, phase contrast.

*Proliferation assay.* The CellTiter 96® AQueous One Solution Cell proliferation Assay (MTS) (Promega; G3580) was used to assess cell proliferation.  $2 \times 10^3$  mPSC1 or 6419c5 cells per well were plated in a 96-well plate approximately 20 hours before adding conditioned media. The growth media were replaced with conditioned and control media, and the cells were allowed to grow for approximately 30 hours. As directed by the manufacturer's protocol, CellTiter 96® AQueous One Solution was added and incubated at 37 °C for 4 hours. Absorbance was recorded at 490nm with a plate reader. Blank-well absorbance was subtracted from the experimental absorbance results.

*Wound healing assay.*  $2.5 \times 10^3$  mPSC1 or  $7 \times 10^3$  6419c5 cells were plated in a 96-well EssenLock plate. At 90-100% confluency, Mitomycin C (10 ng/mL) was added and incubated at 37 °C for 2 hours. Cells were then carefully washed with 1X PBS (+Ca<sup>2+</sup>;+Mg<sup>2+</sup>). Wells were scratched with a uniform cell scratcher, treatments were applied, and cells were placed in the Incucyte System for scanning every 3 hours. Quantification was performed using ImageJ. Recombinant Sema3c (murine, R&D Systems; 1728-S3 and human, R&D Systems; 5570-S3) was administered at 0.1, 0.5, 1 and 2 ug/ml.

*Cell adhesion assay.* The CytoSelect 48-well Cell Adhesion Assay (ECM Array, Colorimetric, Cell Biolabs; CBA-070) was used to quantify cell adhesion. The manufacturer's protocol was followed.  $0.357 \times 10^5$  mPSC1 cells (control and SCG media-treated) were added and incubated for 90 minutes at 37 °C. Cells were carefully washed, treated with the Cell Stain Solution, washed again, and then treated with the Extraction Solution. Absorbance was recorded at 560nm with a plate reader.

*Cytokine array.* The Proteome Profiler Mouse XL Cytokine Array (R&D Systems; ARY028) protocol was followed as described by the manufacturer. Membranes were prepared and each treated with conditioned media filtered with Amicon Centrifugal Filter Units, 50 KDa. Blots were imaged using a chemiluminescence imager, quantified with ImageJ, and plotted using Morpheus (<https://software.broadinstitute.org/morpheus/>)

*Bulk RNA sequencing: RNA preparation, library preparation, and sequencing.* Total RNA was purified using the RNeasy Kit (Qiagen; 74004). β-Mercaptoethanol (β-ME) was used as the reducing agent, and RNA extraction was performed according to the Qiagen protocol. RNA concentration and integrity were verified using a bioanalyzer, and 50 million read pairs per library were prepared and sequenced by the Massively Parallel Sequencing Shared Resource at OHSU.

*Data alignment and preprocessing.* Sequencing data alignment and quantification were performed with STAR (v.2.7.10b) (84). FASTQ files containing sequencing reads for each sample were aligned to the mouse genome assembly GRCm39. STAR alignment options were set to standard ENCODE parameters as detailed in the STAR manual. Gene-level quantification was performed by setting STAR quantification mode to “GeneCounts” and used the GENCODE primary assembly basic genome annotation (M33) (85). Stranded reads for each gene were collected into separate counts matrices representing PSC and nerve samples. One sample representing nerves treated with PSC media was excluded from further analysis due to being the only RNA-seq technical replicate in this work.

*RNA-seq analysis.* All post-alignment RNA-seq data analysis and visualization were performed in R (v.4.2.2) (86). For differential expression analysis, the standard DESeq2 (v.1.38.3) (87) workflow was applied to PSC samples and nerve samples separately. DESeq2 two-factor modeling was used to compare experimental groups while accounting for the experimental batch as a covariate (6/5/2023, 7/5/2023, 8/11/2023, and 9/5/2023). Genes whose read count was cumulatively less than 10 across samples were excluded from differential expression testing in addition to the default DESeq2 low read count gene filter. PCA analysis used read counts that were modified by DESeq2 variance-stabilizing transformation (VST) and subsequently batch-corrected with limma (v3.54.2) (88). Heatmap visualizations of DESeq2 results were generated with pheatmap (v1.0.12) using VST batch-corrected counts and set to scale data by row.

*Gene set enrichment analysis.* Differentially expressed genes from the DESeq2 analysis were input into the GSEA Molecular Signatures Database (MSigDB) gene set enrichment analysis (<https://www.gsea-msigdb.org/gsea/msigdb>). Mouse molecular signatures collections, including hallmark gene sets (MH) and GO Biological Processes (M5, BP), were used to evaluate categorization.

*Reproducibility and statistical analysis.* Sample sizes and replicates were reported. Statistical analyses were primarily performed using GraphPad Prism software (Version 10.4.0(527)). The unpaired two-tailed *t* test was used when comparing parametric data between two groups. ANOVA was performed for multiple conditions. *P* < 0.05 was considered statistically significant.

*Study approval.*

*Human tissue samples.* Human PDAC patient tissue samples and informed consent were obtained from the OPTR [Institutional Review Board (IRB) approved, STUDY00003609]. All methods were carried out in strict compliance with the ethical regulations of the IRB and the institution. Samples were derived from formalin0fixed paraffin embedded (FFPE) primary tumors that underwent pathological review. Tumor-rich

areas were macrodissected for nucleic acid extraction and RNA sequencing. Pathology review was performed at OHSU, and RNA extraction and sequencing were conducted by Tempus (GEO accession: GSE205154).

*Animal studies.* Studies were approved by the Institutional Animal Care and Use Committee (IACUC) at Oregon Health & Science University (OHSU), which reviewed and oversaw each animal model experiment in accordance with NIH guidelines for the humane treatment of animals.

### **Data availability**

All sequencing data from this study have been deposited in the publicly available GEO (GSE318481): <https://www.ncbi.nlm.nih.gov/geo/query/acc.cgi?acc=GSE318481>

## **Author Contributions**

A.L.S. conducted all experiments in the manuscript with support from P.D., J.G., T.K., B.C., and M.J.K.. K.M.H analyzed the bulk RNA-sequencing data. C.P. analyzed survival data from the OPTR with support from R.S.C.. A.L.S., M.H.S., D.L.M., T.A.Z., and S.E.E. designed the experiments and drew conclusions from the data. S.E.E. supervised all experiments and analyses. A.L.S. and S.E.E. wrote the manuscript with input from all authors.

## **Funding Support**

This work is the result of NIH funding, in whole or in part, and is subject to the NIH Public Access Policy. Through acceptance of this federal funding, the NIH has been given a right to make the work publicly available in PubMed Central.

- NIH grants R01 CA257452 (D.L.M., T.A.Z.), R01 CA250917 and Memorial Sloan Kettering Cancer Center P30 CA008748 (M.H.S).
- Cancer Early Detection Advanced Research Center (CEDAR), Project ID# Faculty Startup 2023-1768, Project ID# Exploratory Grant 2025-2044 & 2023-1840 (S.E.E.).
- Oregon Health & Science University, Knight Cancer Institute's Scientific Operations Collaborative Grant (A.L.S.).

## Acknowledgments

We thank all members of the Eksi, Zimmers, Sherman, Langer, Sears, Habecker, Wright, and Grossberg Labs at Oregon Health & Science University for resources and helpful conceptual input on this work. We thank Dr. Kevin Wright for guidance on SCG dissections and Dr. Rosemary Makar for pathological review of tumor specimens. We thank Drs. Rosalie Sears, Dove Keith, Sydney Owens, Alison Grossblatt-Wait, Jason Link, and Terry Morgan of the Oregon Pancreatic Tissue Registry and the Brenden-Colson Center for Pancreatic Care for patient data/specimen collection and curation. This work was supported by the expertise of the OHSU Knight BioLibrary, Massively Parallel Sequencing Shared Resource, Advanced Light Microscopy Shared Resource (RRID:SCR\_009961), and Histopathology Shared Resource (NCI Cancer Center Support, P30 CA069533).

## References

1. Oya Y, Hayakawa Y, Koike K. Tumor microenvironment in gastric cancers. *Cancer Sci.* 2020;111(8):2696–2707.
2. Blondy S, et al. Neurotrophins and their involvement in digestive cancers. *Cell Death Dis.* 2019;10(2):1–12.
3. Saloman JL, et al. Ablation of sensory neurons in a genetic model of pancreatic ductal adenocarcinoma slows initiation and progression of cancer. *Proc Natl Acad Sci U S A.* 2016;113(11):3078–3083.
4. Renz BW, et al. Cholinergic Signaling via Muscarinic Receptors Directly and Indirectly Suppresses Pancreatic Tumorigenesis and Cancer Stemness. *Cancer Discov.* 2018;8(11):1458–1473.
5. Guillot J, et al. Sympathetic axonal sprouting induces changes in macrophage populations and protects against pancreatic cancer. *bioRxiv.* 2020;2020.04.27.061648.

6. Ferdoushi A, et al. Tumor innervation and clinical outcome in pancreatic cancer. *Sci Rep*. 2021;11(1):7390.
7. Chatterjee D, et al. Perineural and Intra-neural Invasion in Posttherapy Pancreaticoduodenectomy Specimens Predicts Poor Prognosis in Patients with Pancreatic Ductal Adenocarcinoma. *Am J Surg Pathol*. 2012;36(3):409–417.
8. Schorn S, et al. Neural invasion severity is a strong predictor of local recurrence in pancreatic ductal adenocarcinoma. *Surgery*. 2025;180:109018.
9. Godoy LD, et al. A Comprehensive Overview on Stress Neurobiology: Basic Concepts and Clinical Implications. *Front Behav Neurosci*. 2018;12:127.
10. Târtea E-A, et al. Clinical Outcomes Depending on Sympathetic Innervation in Pancreatic Cancer. *Cancers*. 2023;15(11):3040.
11. Zahalka AH, et al. Adrenergic nerves activate an angio-metabolic switch in prostate cancer. *Science*. 2017;358(6361):321–326.
12. Huang X, et al. Norepinephrine stimulates pancreatic cancer cell proliferation, migration and invasion via  $\beta$ -adrenergic receptor-dependent activation of P38/MAPK pathway. *Hepatogastroenterology*. 2012;59(115):889–893.
13. Globig A-M, et al. The  $\beta$ 1-adrenergic receptor links sympathetic nerves to T cell exhaustion. *Nature*. 2023;622(7982):383–392.
14. Thiel V, et al. Characterization of single neurons reprogrammed by pancreatic cancer. *Nature*. [published online ahead of print: February 17, 2025]. <https://doi.org/10.1038/s41586-025-08735-3>.

15. Manoukian P, Bijlsma M, van Laarhoven H. The Cellular Origins of Cancer-Associated Fibroblasts and Their Opposing Contributions to Pancreatic Cancer Growth. *Front Cell Dev Biol.* 2021;9:743907.
16. Gascard P, Tlsty TD. Carcinoma-associated fibroblasts: orchestrating the composition of malignancy. *Genes Dev.* 2016;30(9):1002–1019.
17. Öhlund D, Elyada E, Tuveson D. Fibroblast heterogeneity in the cancer wound. *J Exp Med.* 2014;211(8):1503–1523.
18. Öhlund D, et al. Distinct populations of inflammatory fibroblasts and myofibroblasts in pancreatic cancer. *J Exp Med.* 2017;214(3):579–596.
19. Elyada E, et al. Cross-Species Single-Cell Analysis of Pancreatic Ductal Adenocarcinoma Reveals Antigen-Presenting Cancer-Associated Fibroblasts. *Cancer Discov.* 2019;9(8):1102–1123.
20. Auciello FR, et al. A Stromal Lysolipid-Autotaxin Signaling Axis Promotes Pancreatic Tumor Progression. *Cancer Discov.* 2019;9(5):617–627.
21. Francescone R, et al. Netrin G1 promotes pancreatic tumorigenesis through cancer associated fibroblast driven nutritional support and immunosuppression. *Cancer Discov.* 2021;11(2):446–479.
22. Goulet CR, et al. Cancer-associated fibroblasts induce epithelial–mesenchymal transition of bladder cancer cells through paracrine IL-6 signalling. *BMC Cancer.* 2019;19(1):137.
23. Wang F-T, et al. Cancer-associated fibroblast regulation of tumor neo-angiogenesis as a therapeutic target in cancer. *Oncol Lett.* 2019;17(3):3055–3065.
24. Erdogan B, Webb DJ. Cancer-associated fibroblasts modulate growth factor signaling and extracellular matrix remodeling to regulate tumor metastasis. *Biochem Soc Trans.* 2017;45(1):229–236.

25. Kobayashi H, et al. Neuro-Mesenchymal Interaction Mediated by a  $\beta$ 2-Adrenergic Nerve Growth Factor Feedforward Loop Promotes Colorectal Cancer Progression. *Cancer Discov*;OF1–OF25.
26. Roman J. Fibroblasts—Warriors at the Intersection of Wound Healing and Disrepair. *Biomolecules*. 2023;13(6):945.
27. Ivanov E, et al. Sympathetic System in Wound Healing: Multistage Control in Normal and Diabetic Skin. *Int J Mol Sci*. 2023;24(3):2045.
28. Zhang W, et al. Roles of Fibroblast Growth Factors in the Axon Guidance. *Int J Mol Sci*. 2023;24(12):10292.
29. Zhou X, et al. FAP positive cancer-associated fibroblasts promote tumor progression and radioresistance in esophageal squamous cell carcinoma by transferring exosomal lncRNA AFAP1-AS1. *Mol Carcinog*. 2024;63(10):1922–1937.
30. Sherman MH. Stellate Cells in Tissue Repair, Inflammation, and Cancer. 2018;25.
31. Maden M. Retinoic acid in the development, regeneration and maintenance of the nervous system. *Nat Rev Neurosci*. 2007;8(10):755–765.
32. Bressy C, et al. LIF Drives Neural Remodeling in Pancreatic Cancer and Offers a New Candidate Biomarker. *Cancer Res*. 2018;78(4):909–921.
33. Zheng S, et al. Extracellular vesicle-packaged PIAT from cancer-associated fibroblasts drives neural remodeling by mediating m5C modification in pancreatic cancer mouse models. *Sci Transl Med*. 2024;16(756):eadi0178.

34. Helms EJ, et al. Mesenchymal Lineage Heterogeneity Underlies Nonredundant Functions of Pancreatic Cancer–Associated Fibroblasts. *Cancer Discov.* [published online ahead of print: October 14, 2021]. <https://doi.org/10.1158/2159-8290.CD-21-0601>.
35. Secq V, et al. Stromal SLIT2 impacts on pancreatic cancer-associated neural remodeling. *Cell Death Dis.* 2015;6(1):e1592.
36. Lu G, et al. Cancer associated fibroblast derived SLIT2 drives gastric cancer cell metastasis by activating NEK9. *Cell Death Dis.* 2023;14(7):421.
37. Hwang WL, et al. Single-nucleus and spatial transcriptome profiling of pancreatic cancer identifies multicellular dynamics associated with neoadjuvant treatment. *Nat Genet.* 2022;54(8):1178–1191.
38. Maningat AL, Munakomi S. Neuroanatomy, Superior Cervical Ganglion. *StatPearls*. Treasure Island (FL): StatPearls Publishing; 2025.
39. Link JM, et al. Ongoing replication stress tolerance and clonal T cell responses distinguish liver and lung recurrence and outcomes in pancreatic cancer. *Nat Cancer.* 2025;6(1):123–144.
40. Weitz J, et al. Pancreatic ductal adenocarcinoma induces neural injury that promotes a transcriptomic and functional repair signature by peripheral neuroglia. *Oncogene.* 2023;42(34):2536–2546.
41. Hingorani SR, et al. Trp53R172H and KrasG12D cooperate to promote chromosomal instability and widely metastatic pancreatic ductal adenocarcinoma in mice. *Cancer Cell.* 2005;7(5):469–483.
42. Djurec M, et al. Saa3 is a key mediator of the protumorigenic properties of cancer-associated fibroblasts in pancreatic tumors. *Proc Natl Acad Sci U S A.* 2018;115(6):E1147–E1156.

43. Li J, et al. Tumor Cell-Intrinsic Factors Underlie Heterogeneity of Immune Cell Infiltration and Response to Immunotherapy. *Immunity*. 2018;49(1):178-193.e7.
44. Lupo F, et al. Axon guidance cue SEMA3A promotes the aggressive phenotype of basal-like PDAC. *Gut*. 2024;73(8):1321–1335.
45. Jurcak NR, et al. Axon Guidance Molecules Promote Perineural Invasion and Metastasis of Orthotopic Pancreatic Tumors in Mice. *Gastroenterology*. 2019;157(3):838-850.e6.
46. Renz BW, et al.  $\beta$ 2 adrenergic-neurotrophin feed-forward loop promotes pancreatic cancer. *Cancer Cell*. 2018;33(1):75-90.e7.
47. Khan ZU, et al. Chapter One - Memory Deficits in Aging and Neurological Diseases. In: Khan ZU, Muly EC, eds. *Progress in Molecular Biology and Translational Science*. Academic Press; 2014:1–29.
48. Dudgeon C, et al. Netrin-1 feedforward mechanism promotes pancreatic cancer liver metastasis via hepatic stellate cell activation, retinoid, and ELF3 signaling. *Cell Rep*. 2023;42(11):113369.
49. Winkler J, et al. Concepts of extracellular matrix remodelling in tumour progression and metastasis. *Nat Commun*. 2020;11:5120.
50. Tomizawa S, et al. Semaphorin 3 C enhances putative cancer stemness and accelerates peritoneal dissemination in pancreatic cancer. *Cancer Cell Int*. 2023;23(1):155.
51. Tam KJ, et al. Semaphorin 3 C drives epithelial-to-mesenchymal transition, invasiveness, and stem-like characteristics in prostate cells. *Sci Rep*. 2017;7(1):11501.
52. Zhu X, et al. Silencing of semaphorin 3C suppresses cell proliferation and migration in MCF-7 breast cancer cells. *Oncol Lett*. 2017;14(5):5913–5917.

53. Huang W, Yi S, Zhao L. Genetic Features of Young and Aged Animals After Peripheral Nerve Injury: Implications for Diminished Regeneration Capacity. *Cell Mol Neurobiol.* 2023;43(8):4363–4375.
54. Chang JY, Martin DP, Johnson EM. Interferon suppresses sympathetic neuronal cell death caused by nerve growth factor deprivation. *J Neurochem.* 1990;55(2):436–445.
55. Wu L, et al. Molecular and cellular mechanisms underlying peripheral nerve injury-induced cellular ecological shifts: Implications for neuroregeneration. *IBRO Neurosci Rep.* 2025;18:120–129.
56. Navarro X, Vivó M, Valero-Cabré A. Neural plasticity after peripheral nerve injury and regeneration. *Prog Neurobiol.* 2007;82(4):163–201.
57. Bolívar S, et al. Neuron-specific RNA-sequencing reveals different responses in peripheral neurons after nerve injury. *eLife.* 2024;12:RP91316.
58. Belin S, et al. Injury-induced decline of intrinsic regenerative ability revealed by quantitative proteomics. *Neuron.* 2015;86(4):1000–1014.
59. Norrmén C, et al. mTORC1 Is Transiently Reactivated in Injured Nerves to Promote c-Jun Elevation and Schwann Cell Dedifferentiation. *J Neurosci.* 2018;38(20):4811–4828.
60. März P, et al. Sympathetic neurons can produce and respond to interleukin 6. *Proc Natl Acad Sci.* 1998;95(6):3251–3256.
61. Wu Z, et al. Motor neurons transplantation alleviates neurofibrogenesis during chronic degeneration by reversibly regulating Schwann cells epithelial-mesenchymal transition. *Exp Neurol.* 2023;359:114272.
62. Li F, et al. Eosinophilic inflammation promotes CCL6-dependent metastatic tumor growth. *Sci Adv.* 2021;7(22):eabb5943.

63. Poruk KE, et al. Serum Platelet Factor 4 is an Independent Predictor of Survival and Venous Thromboembolism in Patients with Pancreatic Adenocarcinoma. *Cancer Epidemiol Biomark Prev Publ Am Assoc Cancer Res Cosponsored Am Soc Prev Oncol*. 2010;19(10):2605–2610.
64. Sun X, et al. Inflammatory cell-derived CXCL3 promotes pancreatic cancer metastasis through a novel myofibroblast-hijacked cancer escape mechanism. *Gut*. 2022;71(1):129–147.
65. Lunardi S, et al. IP-10/CXCL10 induction in human pancreatic cancer stroma influences lymphocytes recruitment and correlates with poor survival. *Oncotarget*. 2014;5(22):11064–11080.
66. Gao H-F, et al. CXCL9 chemokine promotes the progression of human pancreatic adenocarcinoma through STAT3-dependent cytotoxic T lymphocyte suppression. *Aging*. 2020;12(1):502–517.
67. Picklo MJ. Methods of sympathetic degeneration and alteration. *J Auton Nerv Syst*. 1997;62(3):111–125.
68. Imrie CW. Denervation Procedures in the Management of Chronic Pancreatitis. In: Beger HG, et al., eds. *Chronic Pancreatitis*. Berlin, Heidelberg: Springer; 1990:411–414.
69. Pereira MMA, et al. A brain-sparing diphtheria toxin for chemical genetic ablation of peripheral cell lineages. *Nat Commun*. 2017;8(1):14967.
70. Erstad DJ, et al. Orthotopic and heterotopic murine models of pancreatic cancer and their different responses to FOLFIRINOX chemotherapy. *Dis Model Mech*. 2018;11(7):dmm034793.
71. Kim S-N, et al. Sex differences in sympathetic innervation and browning of white adipose tissue of mice. *Biol Sex Differ*. 2016;7:67.

72. Stephens KE, et al. Sex differences in gene regulation in the dorsal root ganglion after nerve injury. *BMC Genomics*. 2019;20(1):147.
73. Perez SD, et al. Sympathetic Innervation of the Spleen in Male Brown Norway Rats: A Longitudinal Aging Study. *Brain Res*. 2009;1302:106–117.
74. Bouman A, Heineman MJ, Faas MM. Sex hormones and the immune response in humans. *Hum Reprod Update*. 2005;11(4):411–423.
75. Gaillard RC, Spinedi E. Sex- and stress-steroids interactions and the immune system: evidence for a neuroendocrine-immunological sexual dimorphism. *Domest Anim Endocrinol*. 1998;15(5):345–352.
76. Elinos D, et al. Segregation of Acetylcholine and GABA in the Rat Superior Cervical Ganglia: Functional Correlation. *Front Cell Neurosci*. 2016;10. <https://doi.org/10.3389/fncel.2016.00091>.
77. Kanda H, et al. The neuronal and glial cell diversity in the celiac ganglion revealed by single-nucleus RNA sequencing. *Sci Rep*. 2025;15(1):5510.
78. Casais M, et al. The celiac ganglion modulates LH-induced inhibition of androstenedione release in late pregnant rat ovaries. *Reprod Biol Endocrinol*. 2006;4(1):66.
79. Xu X, et al. Increased semaphorin 3c expression promotes tumor growth and metastasis in pancreatic ductal adenocarcinoma by activating the ERK1/2 signaling pathway. *Cancer Lett*. 2017;397:12–22.
80. Boeshore KL, et al. Novel changes in gene expression following axotomy of a sympathetic ganglion: a microarray analysis. *J Neurobiol*. 2004;59(2):216–235.
81. Jackson M, Tourtellotte W. Neuron Culture from Mouse Superior Cervical Ganglion. *Bio-Protoc*. 2014;4(2):e1035.

82. Renier N, et al. iDISCO: A Simple, Rapid Method to Immunolabel Large Tissue Samples for Volume Imaging. *Cell*. 2014;159(4):896–910.
83. Hsu C-W, et al. EZ Clear for simple, rapid, and robust mouse whole organ clearing. *eLife*. 2022;11:e77419.
84. Dobin A, et al. STAR: ultrafast universal RNA-seq aligner. *Bioinformatics*. 2013;29(1):15–21.
85. GENCODE 2025: reference gene annotation for human and mouse | Nucleic Acids Research | Oxford Academic [Internet]. <https://academic.oup.com/nar/article/53/D1/D966/7905300>. Accessed February 17, 2025.
86. R: The R Project for Statistical Computing [Internet]. <https://www.r-project.org/>. Accessed February 17, 2025.
87. Love MI, Huber W, Anders S. Moderated estimation of fold change and dispersion for RNA-seq data with DESeq2. *Genome Biol*. 2014;15(12):550.
88. Ritchie ME, et al. limma powers differential expression analyses for RNA-sequencing and microarray studies. *Nucleic Acids Res*. 2015;43(7):e47.

## Figure Legends

**Figure 1. Human and murine PDAC tumors are innervated by autonomic nerves.** (A) Co-immunofluorescent image of an intratumoral nerve bundle in human PDAC stained with VACHT (green), TH (white), and DAPI (cyan), alongside the matched H&E image. Scale bar: 100  $\mu$ m. (B) Kaplan-Meier estimates of overall survival in patients with PDAC, stratified by primary tumor high or low gene expression of *TUBB3*,

*TRPV1*, *VACht*, and *TH* (n = 208). (C) Co-immunofluorescent image of an intratumoral nerve bundle in a murine KPC tumor stained with *VACht* (green), *TH* (white), and DAPI (cyan), alongside the matched H&E image. Scale bar: 50  $\mu\text{m}$ . (D) Representative cleared KPC tumors stained with *TH* (white). Red brackets mark tumor-encasing nerves, and blue arrows mark tumor-invading nerves. Scale bars: 500  $\mu\text{m}$  and 1000  $\mu\text{m}$ .

**Figure 2. Intratumor sympathetic nerves are closely associated with CAFs.** Representative co-immunofluorescent images of (A) human and (B) murine PDAC marked with *TH* (white), alpha-smooth muscle actin (*aSMA*) (magenta), and DAPI (cyan). Scale bars: 50  $\mu\text{m}$  and 100  $\mu\text{m}$ .

**Figure 3. Pancreas-specific genetic sympathectomy sympathetic innervation.** (A) Representative immunofluorescent image of SCG outgrowth marked with *Dbh* (white), and neurofilament medium (*NF-m*) (red). Scale bars: 100  $\mu\text{m}$ . (B) Schematic of murine genetic sympathectomy model. Homozygous *Rosa26-iDTR* mice were crossed with heterozygous *Dbh-Cre* mice, resulting in offspring comprised of 50% *Rosa26-iDTR*; *Dbh-WT* (control group) and 50% *Rosa26-iDTR*; *Dbh-Cre* (ablation group). (C) Representative immunofluorescent images validating healthy pancreas sympathetic ablations with low (100 ng), mid (250 ng), and high (500 ng) DT doses. Each image was acquired with the same exposure and contrast settings; max intensity projections are shown. Scale bars: 200  $\mu\text{m}$ .

**Figure 4. Sympathetic nerves promote female PDAC tumor growth.** (A) Schematic of intra-pancreatic DT injections combined with an orthotopic KPC (6419c5) injection. (B) Representative immunofluorescent staining of sympathetic nerves with *TH* (white) in the tumor-adjacent pancreas of control vs. sympathectomized cohorts. Images acquired with the same exposure and contrast settings; max intensity projections shown. Scale bars: 500  $\mu\text{m}$ . (C) Quantification of normalized *TH*% area (fold change) of control vs. sympathectomized tumor-adjacent pancreas in male (n = 6 control, n = 4 ablation) and female (n = 4 control, n = 5 ablation) mice. Data were normalized to the mean of the control groups across staining batches. Each dot represents one animal, bar plot mean  $\pm$  SD; \**P* < 0.05, \*\*\**P* < 0.001; paired Wilcoxon signed rank test. (D) Combined male (dark blue) and female (light blue) tumor weights (grams) of control and sympathetic ablation groups. Each dot represents one animal, mean  $\pm$  SD; not significant (ns) *P* > 0.05; paired Wilcoxon signed rank test. Endpoint KPC tumor

weights (grams) separated by sex: (E) male (n = 6 control, n = 4 ablation) and (F) female (n = 4 control, n = 5 ablation). Each dot represents one animal, bar plots mean  $\pm$  SD; \*\*\* $P < 0.001$ , \*\*\*\* $P < 0.0001$ ; unpaired, 2-tailed Student's  $t$  test. (G) Representative endpoint tumors of female control and ablated tumors. The tape measure is marked in centimeters (cm). (H) Correlation between female normalized TH percent area compared to KPC orthotopic tumor weights (grams). (I) Schematic of conditioned media proliferation assay. Proliferation of (J) KPC (6419c5) and (K) PSC (mPSC1) cells cultured with SCG-conditioned (+SCG) or control (-SCG) media. n = 8 replicates, bar plots mean  $\pm$  SD; \*\*\* $P < 0.001$ , \*\*\*\* $P < 0.0001$ ; unpaired, 2-tailed Student's  $t$  test.

**Figure 5. Sympathetic nerves drive CAF activation and ECM remodeling.** (A) Schematic of indirect co-culture of PSCs with SCGs. (B) Heatmap of all differentially expressed protein-coding genes in PSC controls compared to PSC+SCG experimental groups. (C) Gene set enrichment analysis (GSEA) normalized enrichment scores (NES) of signaling pathways related to CAF activation (Hallmarks) and extracellular matrix remodeling (GO Biological Processes). (D) Epithelial to mesenchymal transition GSEA plot (NES = 1.71, FDR q-value = 0.007) and top 30 significantly enriched genes. (E) Wound healing assay, % bar plot, and closure curve of PSCs treated with Ctrl and SCG-conditioned media. n = 5 wounds per timepoint, per treatment, mean  $\pm$  SD; ns  $P > 0.05$ , \* $P < 0.05$ , \*\* $P < 0.01$ , \*\*\* $P < 0.001$ ; unpaired, 2-tailed Student's  $t$  test; 2-way ANOVA, repeated measures. (F) IL6 JAK/STAT3 signaling GSEA plot (NES = 1.32, FDR q-value = 0.046) and top 25 significantly enriched genes. Quantified ratio % of iCAF to myCAFs in Ctrl and ablated tumors of (G) female and (H) male mice. (I) Extracellular structure reorganization GSEA plot (NES = 1.74, FDR q-value = 0.19) and top 25 significantly enriched genes. (J) Quantification of ECM (% area) in female tumors. Each dot represents one animal n = 9, bar plot mean  $\pm$  SD; ns  $P > 0.05$ . (K) Adhesion assay of PSCs treated with Ctrl media and SCG-conditioned media. Bar plot. n = 3 wells per ECM scaffolding, mean  $\pm$  SD; ns  $P > 0.05$ , \*\* $P < 0.01$ ; unpaired, 2-tailed Student's  $t$  test.

**Figure 6. Upregulation of Sema3c enhances metastatic phenotypes.** Kaplan-Meier estimates for female PDAC patients stratified by (A) *SEMA3C* and (B) *NRP1* expression. (C) Co-immunofluorescent images of SEMA3C (yellow), PDPN (magenta) and NF-m (green) expressed in PSCs cocultured with SCG media or SCGs directly. Scale bars: 100  $\mu$ m. (D) Intensity sum of SEMA3C expression in PSCs co-cultured with control media, SCG-conditioned media, and directly with SCGs. Each dot represents one cell, bar plot mean  $\pm$  SD; ns  $P > 0.05$ , \*\*\* $P < 0.001$ , \*\*\*\* $P < 0.0001$ . (E) Immunofluorescent staining of NRP1 (yellow) in a human PDAC tumor section. Scale bars: 50  $\mu$ m. (F) Wound healing assay % closure of KPC Cells (6419c5) treated with ctrl

media and recombinant SEMA3C.  $n = 4$  wounds per timepoint, per treatment, mean  $\pm$  SD.  $*P < 0.05$ ; 2-way ANOVA, repeated measures. Mean intensity quantification of immunofluorescent staining of KPC (6419c5) cells with (G) SNAIL/SLUG (H) VIMENTIN and Panc1 cells with (I) SNAIL/SLUG and (J) VIMENTIN.

**Figure 7. Cancer and fibroblast signaling enhances SCG axon outgrowth.** (A) Schematic of indirect co-culture systems. SCG explants (colored yellow) were plated on the bottom of each well (the schematic does not represent the actual number of SCG explants, typically around 8 explants per well). SCG explants were co-cultured either alone (no cells) or with cells on inserts, including MEFs (control fibroblasts, blue), mPSC1 cells (pancreatic-derived CAFs, violet), and 6419c5 KPC cells (orange). (B) Representative phase contrast image of SCG explant radial axon outgrowth at hour 22 and hour 44 post-plating. The yellow outline indicates the edge of measured averaged radial axon outgrowth, and the purple represents average axon traces. Scale bars: 500  $\mu\text{m}$ . (C) Quantification of SCG axon length of explants in co-culture conditions: NA (no cells), MEFs (Ctrl. fibroblasts) PSCs (mPSC1), and KPC cells (6419c5). (Each dot represents one SCG explant, mean  $\pm$  SD;  $*P < 0.05$ ,  $**P < 0.01$ , and  $***P < 0.001$ ; 1-way ANOVA).

**Figure 8. CAF-specific transcriptional effects on SCG explants.** (A) Heatmap of differentially expressed genes comparing SCGs alone (yellow), SCGs co-cultured with MEFs (blue), and PSC cells (purple). The genes shown (rows) are all significant, differentially expressed genes across all condition comparisons. (B) GSEA of SCG+PSC vs. SCG of biological processes enriched gene sets. From top to bottom, select pathways upregulated: cell cycle (green), immune response (orange), metabolic pathways (blue), neuron plasticity (yellow), and injury signaling (pink). (C) Venn diagram of upregulated genes of different co-culture comparisons. Bar graphs delineating specific genes upregulated in (D) both SCG+PSC and SCG+MEF samples and (E) SCG+PSC samples, categorized by nerve injury, ligands, receptors, and transcription factor ( $\log_2$  fold change).

# Figures

Figure 1:

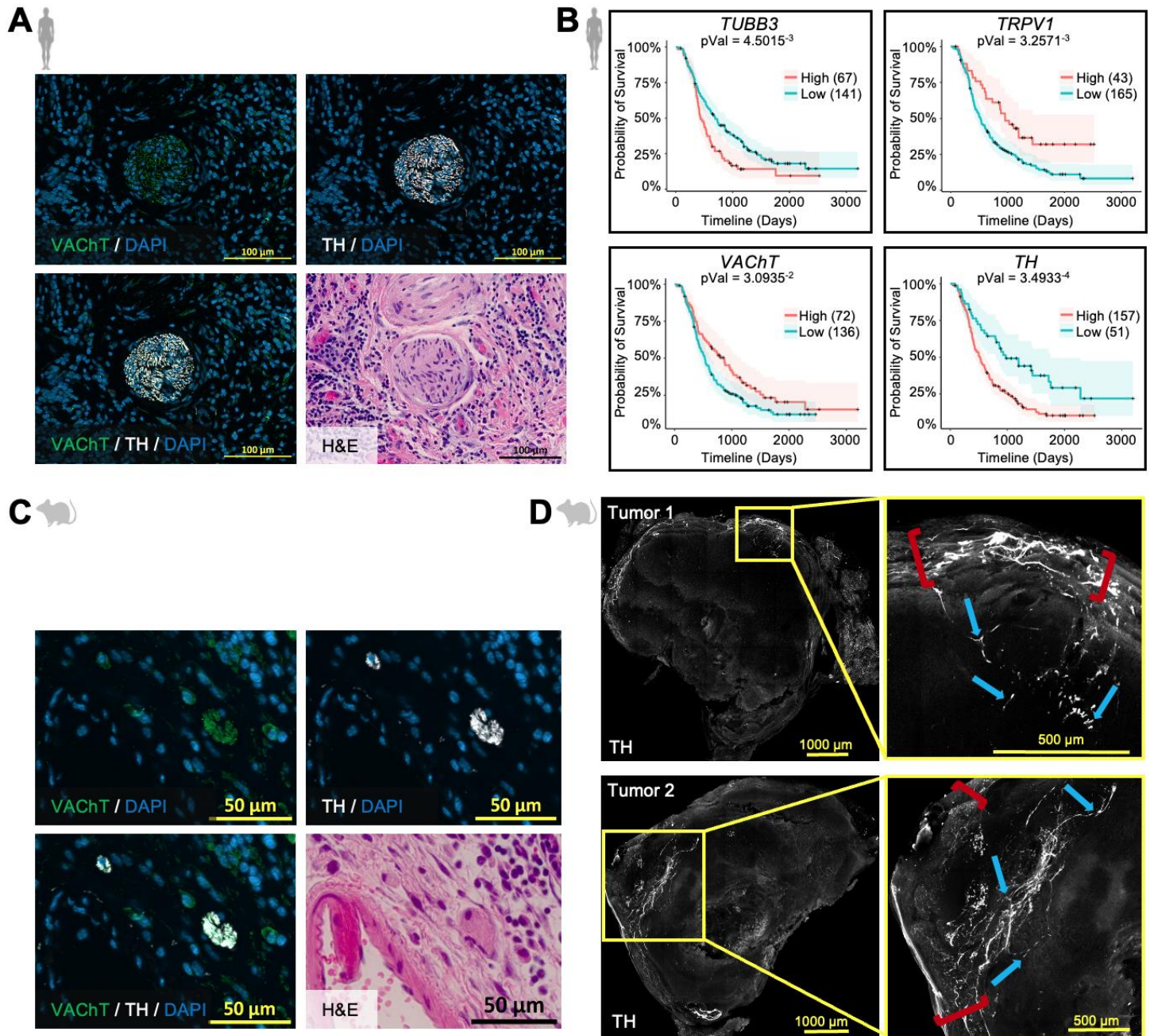


Figure 2:

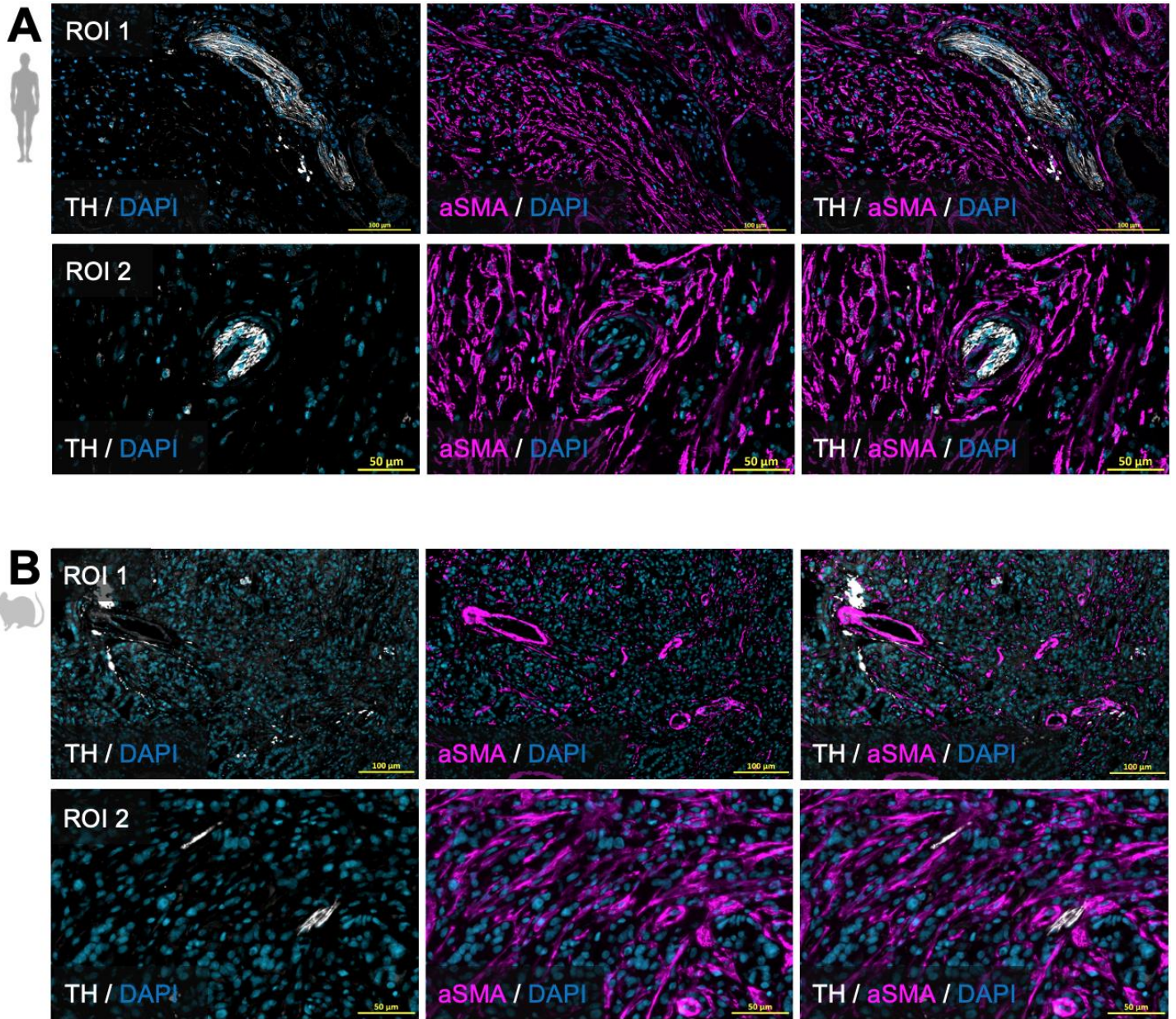


Figure 3:

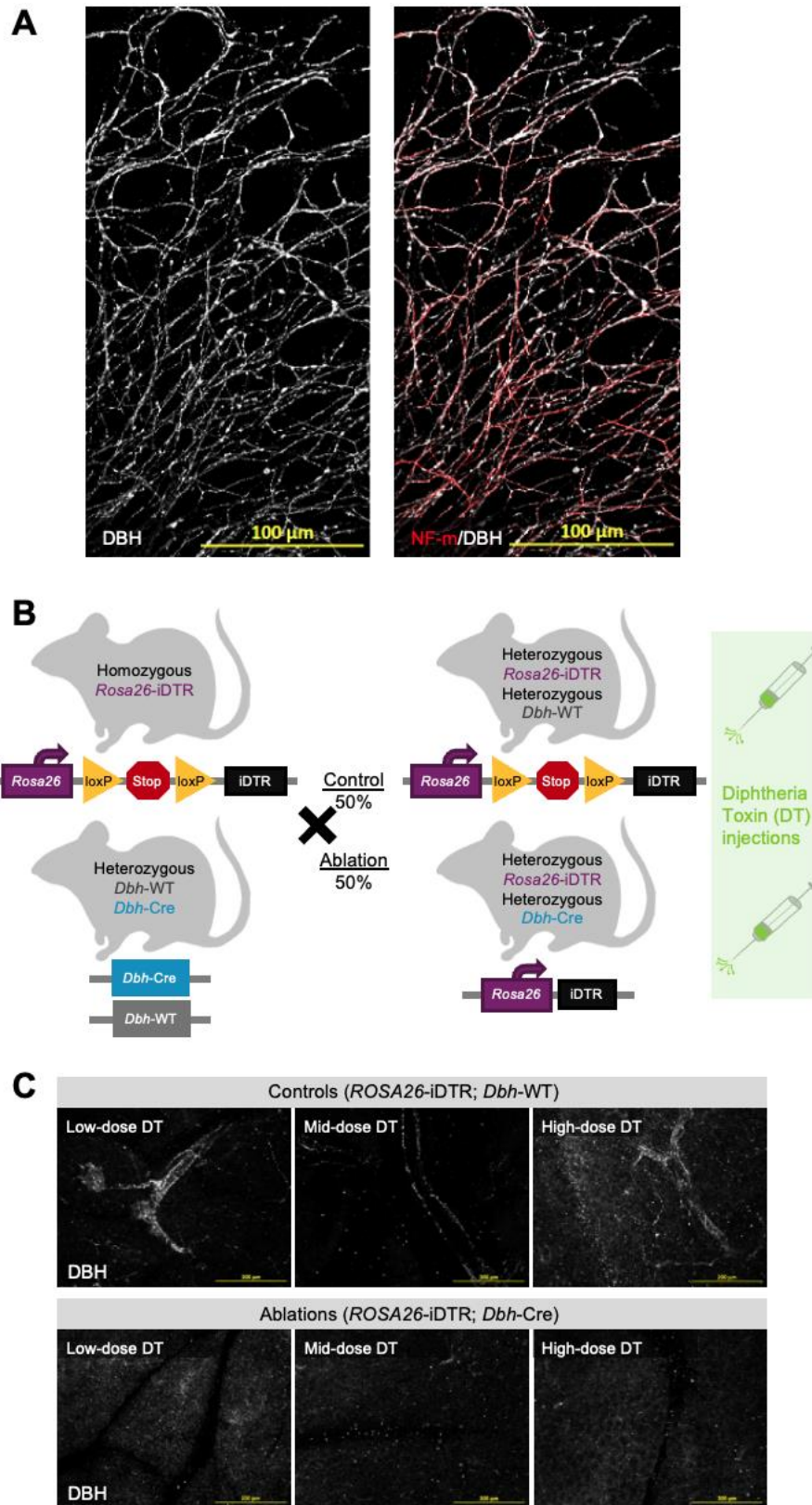


Figure 4:

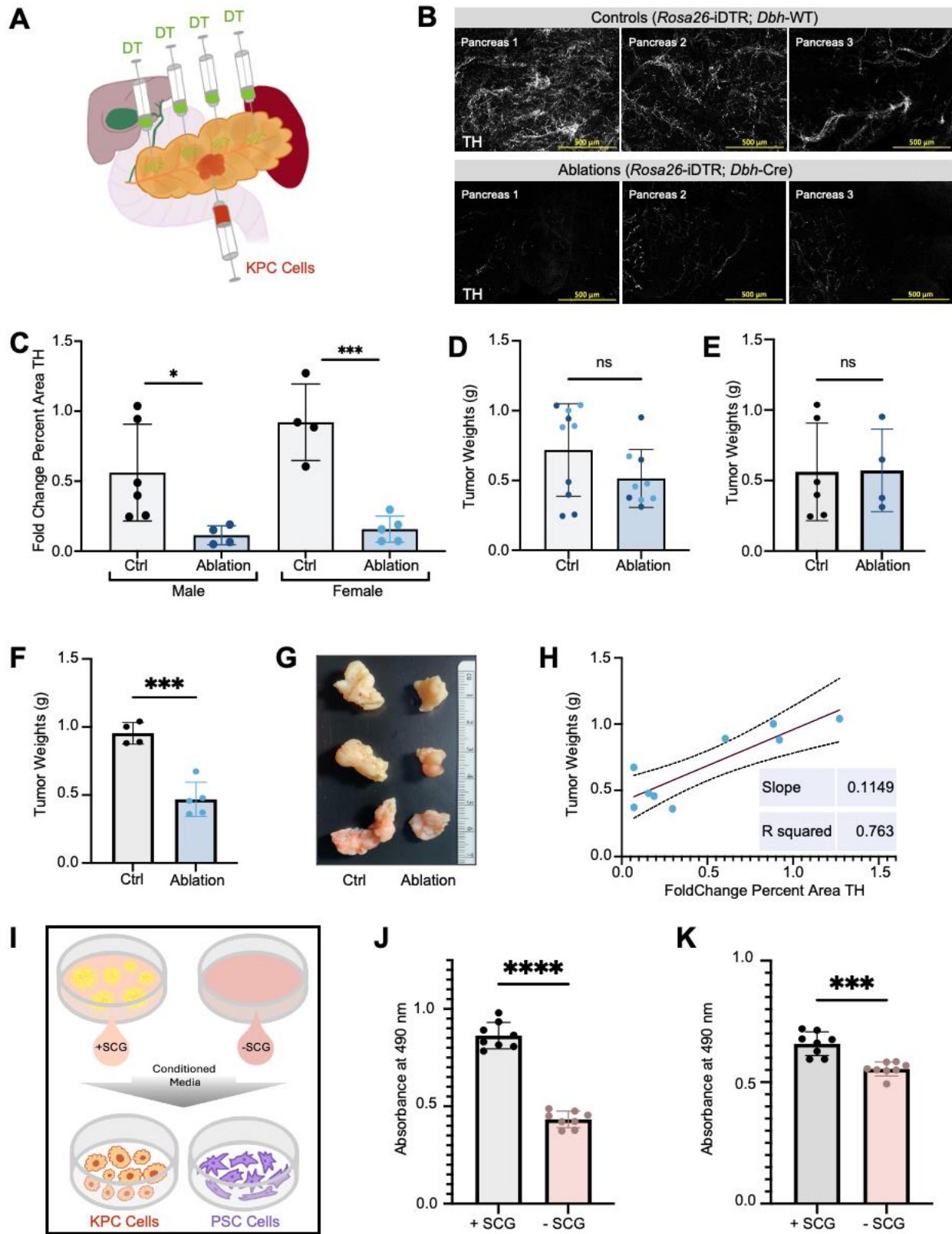
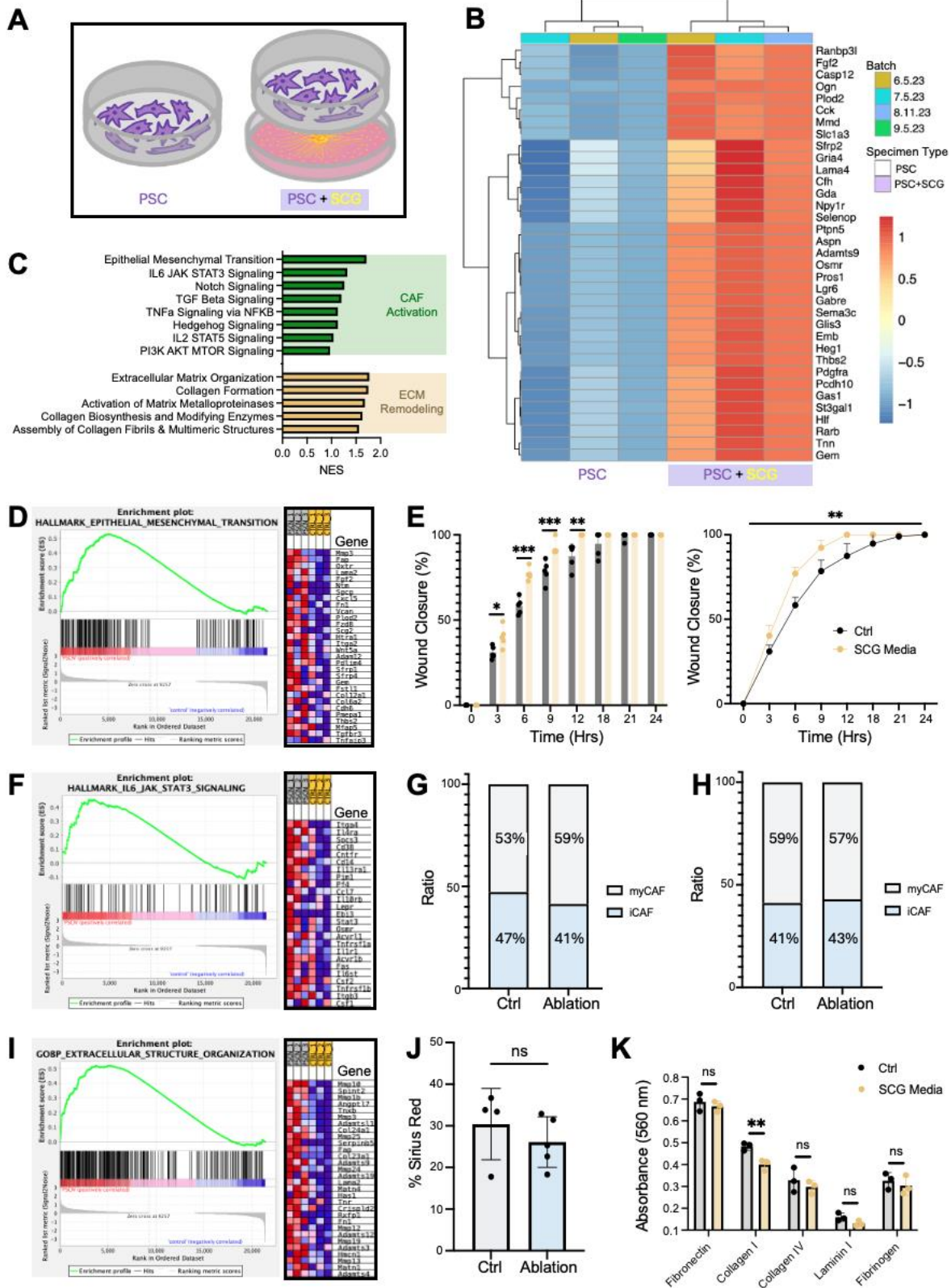


Figure 5:



**Figure 6:**

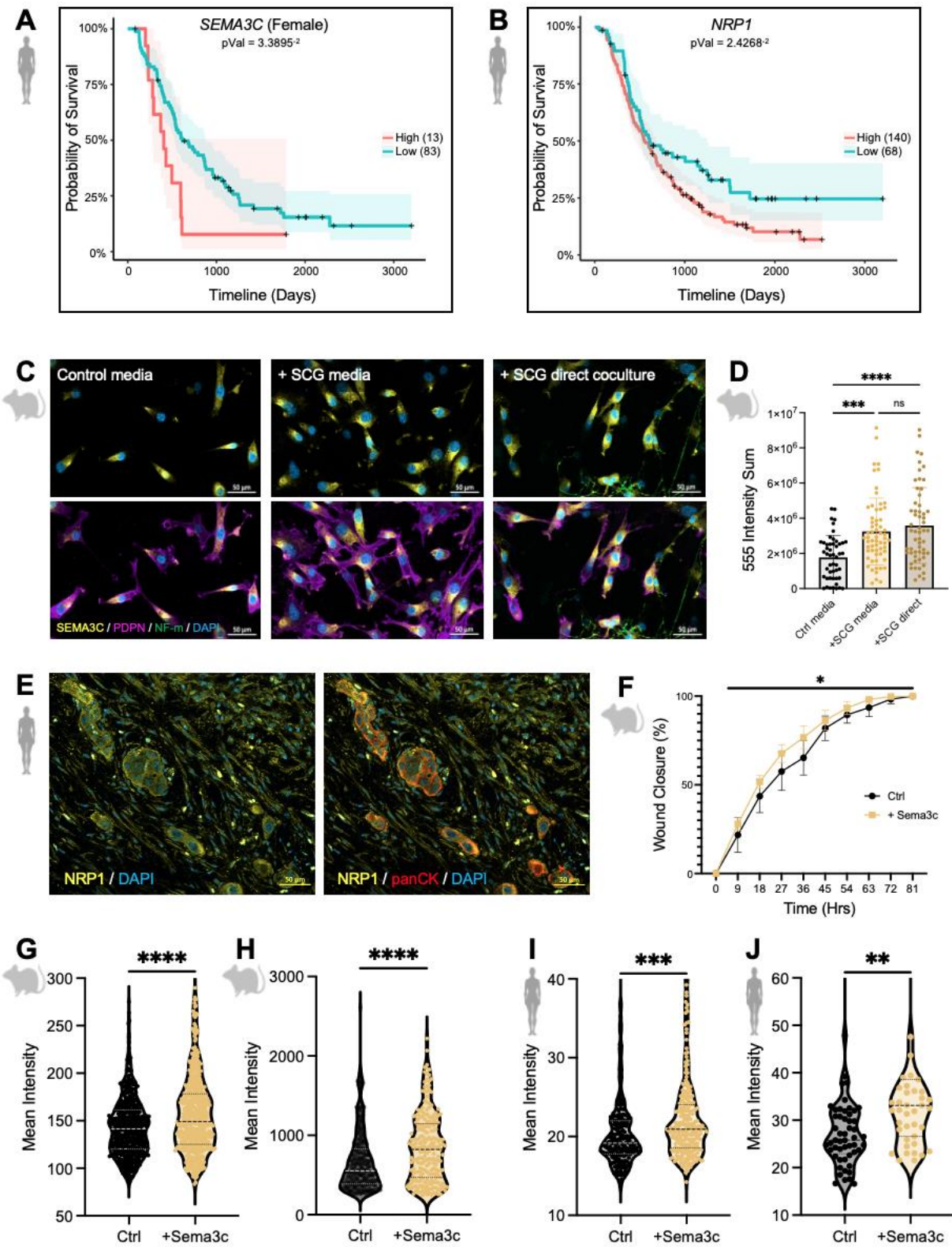


Figure 7:

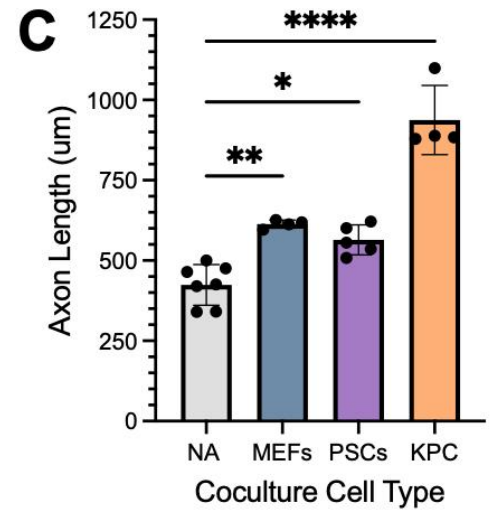
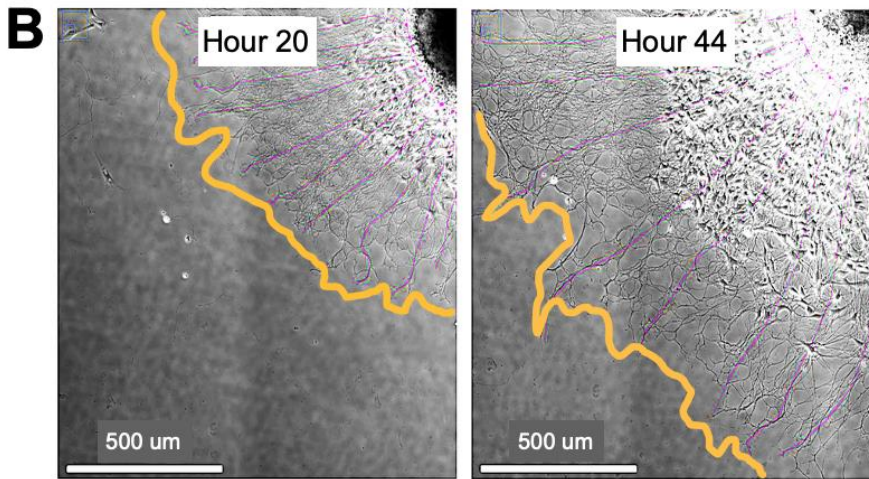
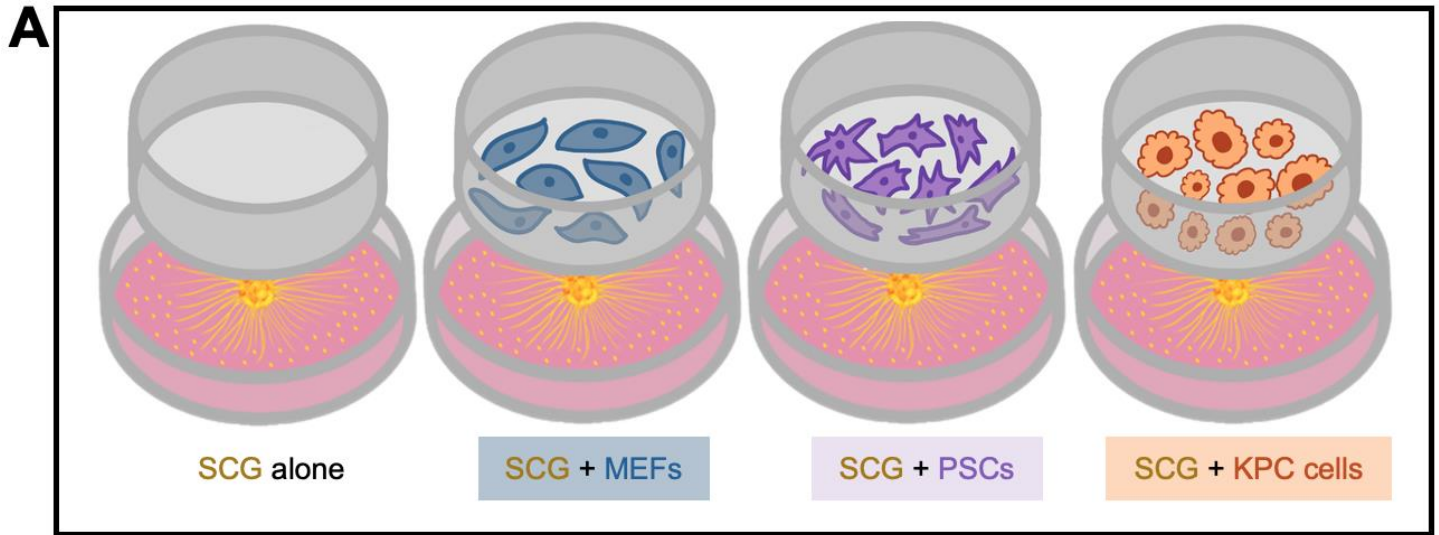


Figure 8:

